Geophysical Journal International

Geophys. J. Int. (2013) doi: 10.1093/gji/ggt151

Geophysical Journal International Advance Access published May 14, 2013

Dynamics of the North American continent

A. Ghosh,[1,*] T. W. Becker[1] and E. D. Humphreys[2]

[1]*Department of Earth Sciences, University of Southern California, Los Angeles, USA. E-mail: attreyeg@usc.edu*
[2]*Department of Geological Sciences, University of Oregon, Eugene, USA*

Accepted 2013 April 12. Received 2013 April 12; in original form 2012 August 17

SUMMARY

The forces that cause deformation of western North America have been debated for decades. Recent studies, primarily based on analysis of crustal stresses in the western United States, have suggested that the deformation of the region is mainly controlled by gravitational potential energy (GPE) variations and boundary loads, with basal tractions due to mantle flow playing a relatively minor role. We address these issues by modelling the deviatoric stress field over western North America from a 3-D finite element mantle circulation model with lateral viscosity variations. Our approach takes into account the contribution from both topography and shallow lithosphere structure (GPE) as well as that from deeper mantle flow in one single model, as opposed to separate lithosphere and circulation models, as has been done so far. In addition to predicting the deviatoric stresses we also jointly fit the constraints of geoid, dynamic topography and plate motion both globally and over North America, in order to ensure that the forces that arise in our models are dynamically consistent. We examine the sensitivity of the dynamic models to different lateral viscosity variations. We find that circulation models that include upper mantle slabs yield a better fit to observed plate velocities. Our results indicate that a model of GPE variations coupled with mantle convection gives the best fit to the observational constraints. We argue that although GPE variations control a large part of the deformation of the western United States, deeper mantle tractions also play a significant role. The average deviatoric stress magnitudes in the western United States range 30–40 MPa. The cratonic region exhibits higher coupling to mantle flow than the rest of the continent. We find that a relatively strong San Andreas fault gives a better fit to the observational constraints, especially that of plate velocity in western North America.

Key words: Numerical solutions; Cratons; Dynamics of lithosphere and mantle; Dynamics: gravity and tectonics; Rheology: mantle; North America.

1 INTRODUCTION

The North American continent is characterized by a stable and relatively flat eastern part underlain by seismically high-velocity cratonic root and a tectonically active, mountainous western part characterized by broadscale slow velocity anomalies in the upper mantle. The Laramide orogeny is mostly responsible for forming the present-day topography of western North America (e.g. Livacarri 1991; Spencer 1996; English & Johnston 2004; Liu *et al.* 2010), although the processes driving orogeny are not well understood. Considering the uncertainty of the nature of thermochemical convection beneath the western United States, a relevant question is how western U.S. deformation is linked to the underlying dynamics of mantle flow. In other words, is western U.S. deformation controlled by lithospheric processes (e.g. Flesch *et al.* 2000, 2007; Humphreys & Coblentz 2007), or by deeper mantle flow, and if mantle tractions are important, do they drive (Bokelmann 2002; Liu & Bird 2002; Becker *et al.* 2006) or resist (Humphreys & Coblentz 2007; Silver & Holt 2002) North American Plate motion? Humphreys & Coblentz (2007) argued that density-driven shear tractions play a role in producing the deformation of North America, but at a reduced scale (∼20 per cent) from those predicted by Becker & O'Connell (2001). Their modelling involved loading a 2-D thin spherical shell representing the North American Plate and inverting for the magnitudes of those loads. They concluded that GPE and boundary loads are the most important forces affecting the North American continent. Moreover, the mantle tractions in their study came from a circulation model with only radial variations of viscosity (Becker & O'Connell 2001). The question remains whether lateral viscosity variations (LVVs), potentially arising from a strong

[*] Now at: Centre for Earth Sciences, Indian Institute of Science, Bangalore, India.

continental keel in the eastern part of the continent (e.g. Conrad & Lithgow-Bertelloni 2006) and weak plate boundary to the west, will change the impact of mantle tractions on the continental stress field. Our goal is to test the findings of Humphreys & Coblentz (2007) in a global 3-D model that is fully dynamically consistent. So far, to our knowledge, no study has explored the dynamic consequences of including lateral strength variations beneath North America.

The dynamics of mantle flow are manifested in a variety of surface geophysical features, such as the Earth's gravity anomalies, dynamic topography, plate motions and the lithospheric deviatoric stress field. Forte *et al.* (2010) have explored the effects of deep mantle flow on surface geophysical observations over North America. They matched gravity anomalies, plate motion and dynamic topography over the continent. However, their models did not include LVVs and since they were only interested in deeper mantle contribution, they did not address the issue of lithosphere versus mantle effects. Moreover, although they studied the deviatoric stress predictions in North America, they did not perform any quantitative analysis on these predictions. The deviatoric stress field can serve as an important constraint of relative viscosity variations in the lithosphere and the mantle (e.g. Ghosh *et al.* 2008, 2013). Where strike-slip faulting dominates, such as along the western margin of North America, lithospheric strength might be mechanically anisotropic. The San Andreas fault (SAF) has often been speculated to be weaker along the direction of shear (Gilbert & Scholz 1994) and the effect of such anisotropic viscosity in western United States has only been considered locally (Jones *et al.* 1996). One of our goals is to examine the impact of an anisotropic SAF on the deviatoric stress field over the western United States.

An important omission from some geodynamic models is a neglect of topography and shallow lithosphere structure that give rise to differences in gravitational potential energy (GPE), which can potentially act as an important component of the global force balance (Husson *et al.* 2008). Several earlier studies have looked at the Earth's lithospheric stress field globally by combining effects of topography and shallow lithosphere structure with basal tractions from mantle flow by computing them separately (Bai *et al.* 1992; Bird 1998; Steinberger *et al.* 2001; Lithgow-Bertelloni & Guynn 2004; Ghosh *et al.* 2008; Naliboff *et al.* 2009; Ghosh & Holt 2012; Ghosh *et al.* 2013). Here, we incorporate the effect of GPE variations and mantle flow in a single calculation. The advantage of calculating the GPE and mantle response in the same calculation is that way we avoid any inconsistency that may arise from having separate models for lithosphere and mantle convection. Moreover, this type of 3-D treatment can alleviate some of the assumptions inherent in thin-sheet models (Flesch *et al.* 2001; Humphreys & Coblentz 2007; Bird *et al.* 2008; Ghosh *et al.* 2009).

The deviatoric stress field over North America, and in particular over the western United States, has been a subject of many previous studies. Humphreys & Coblentz (2007) and Flesch *et al.* (2000, 2007) have argued for a dominance of GPE related stresses over western North America. Wesnousky & Scholz (1980) argued that the presence of craton is responsible for the east–west compressional stresses to the east of the Great Plains and approximately N–S trending tensional stresses to the west. Jones *et al.* (1996) again pointed out the importance of GPE in explaining western U.S. deformation. Sonder & Jones (1999) concluded that much of the western U.S. extension can be attributed to GPE variations, but it is insufficient to explain all of western U.S. extension; horizontal tractions driven by mantle buoyancies play a role. Forte *et al.* (2010) studied the SH_{max} predictions in North America from a density driven global flow model.

In this study, we address the issue of deformation of the western United States with 3-D finite element global mantle circulation models that include LVVs and take into account both deeper mantle and shallow lithospheric contributions. We test our models against deviatoric stress field, long wavelength geoid, dynamic topography and plate motions. These constraints help us to delineate the suitable density and viscosity structures amongst numerous possibilities. Although we are interested in North America, especially western North America, we take a global approach. That is, we attempt to satisfy the observational constraints of geoid, dynamic topography, plate motions and stress field not only over the continent, but globally as well.

2 MANTLE FLOW

We use a version of the finite element software CitcomS (Zhong *et al.* 2000), which we jointly extended with CIG (www.geodynamics.org), to compute the long wavelength geoid, dynamic topography, plate velocities and deviatoric stresses over North America. We solve the equations for instantaneous, incompressible fluid flow with infinite Prandtl number, where flow is driven by mantle density anomalies (Boussinesq approximation). We test various global tomography models including the composite tomography model SMEAN (Becker & Boschi 2002), the *S*-wave tomography model TX2008 (Simmons *et al.* 2007), and *SV* velocity model LH08 (Lebedev & van der Hilst 2008). In addition, we also test a regional model (SH_TX2008) by Schmandt & Humphreys (2010) nested in the global *S*-wave model TX2008 (*cf.* Becker 2012). The regional model is scaled to match the global model's rms in the study area. For all tomography models, the high velocity anomalies above 300 km are removed in cratonic areas to make the keels neutrally buoyant (Jordan 1978; Forte & Perry 2000). We use two different ways to do this, one by using a craton model (Nataf & Ricard 1996), the other by removing high velocity regions within the continents higher than a particular velocity, depending on depth. In addition to the tomography models we also use a regionalized upper mantle (RUM) slab model from Gudmundsson & Sambridge (1998). A velocity-density scaling ($\mathrm{d}\ln\rho/\mathrm{d}\ln v_s$) of 0.25 is used for the *S*-wave tomography models throughout the mantle, for simplicity (see Forte *et al.* 2010, for a discussion).

We experiment with various radial and LVVs. We search a subset of the parameter space and find the radial and lateral viscosity structure that provides the best correlation to global geoid and plate velocities simultaneously (Ghosh *et al.* 2010). We start with a five-layer viscosity structure divided into lithosphere (0–100 km), asthenosphere (100–300 km), upper mantle (300–410 km), transition zone (410–660 km) and lower mantle (660–CMB). Lithosphere viscosities tested are 10–300 times stiffer than reference transition zone viscosity (10^{21} Pa s). The asthenosphere and upper-mantle viscosities are 0.01–1 times the reference viscosity and the lower-mantle viscosities are 10–100 times the reference viscosity. LVVs are introduced by taking into account high-viscosity keels from 3SMAC cratons (Nataf & Ricard 1996) that reach a depth of 300 km, with viscosity ranging from 10 to 1000 times greater than the ambient mantle. LVVs also include weak plate boundaries, ranging from 10 to 1000 times weaker than the lithosphere. In one case, we also use the strain rate dependent viscosities for the plate boundaries based on strain rates of Kreemer *et al.* (2003), after Ghosh *et al.* (2008). We incorporate temperature dependent viscosity

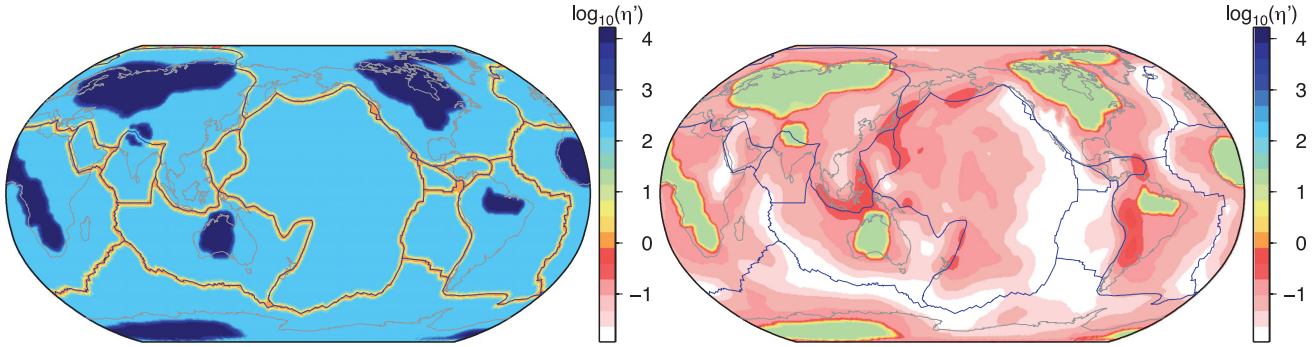

Figure 1. Lateral viscosities in the top 100 km (left-hand side panel), which consists of stiff cratons and weak plate boundaries. Same at a depth of 150 km (right-hand side panel) that includes stiff slabs and temperature dependent viscosity (temperature inferred from tomographic model RUM + SH_TX2008) in addition to keels. Viscosity $\eta' = \eta/\eta_{\rm ref}$, where $\eta_{\rm ref}$ is the reference upper mantle viscosity.

below 100 km depth by allowing viscosity to vary with temperature according to $\eta = \eta_0 \exp(\gamma(T_0 - T))$, where T_0 and T are the reference and non-dimensionalized temperatures; γ determines the strength of temperature dependence. We test γ values of 5, 10 and 30, leading to 2, 4 and 13 orders of magnitude variations as a function of T. The cut-off viscosity values are 3 orders of magnitude lower and 4 orders of magnitude higher than the reference viscosity. The best fitting models, chosen on the basis of yielding a high correlation to the global geoid and plate motions simultaneously, have a stiff lithosphere (150×10^{21} Pa s), weak asthenosphere (0.08×10^{21} Pa s), moderately weak upper mantle (0.3×10^{21} Pa s), weak plate boundaries (1.5×10^{21} Pa s) and strong keels (100 times stronger than the ambient mantle), and a γ value of 10 (Fig. 1). The horizontal resolution used for these tests are $\sim 0.75 \times 0.75^\circ$, although for the final models we use a higher resolution of $\sim 0.25 \times 0.25^\circ$. Models are run with free slip boundary condition at the surface except those where we include the effect of GPE as discussed later, and at core–mantle boundary.

For comparison, we use the geoid from Mayer-Guerr (2006) corrected for the hydrostatic shape of the Earth following Nakiboglu (1982) (Figs 2a and 3a). We also tested the geoid, which was a correction of the Nakiboglu (1982) geoid values by Chambat *et al.* (2010). However, differences in correlation are less than 1 per cent using the corrected values compared to those from Nakiboglu (1982). The predicted geoid is computed up to spherical harmonic degree 63, including the effects of self-gravitation. The global correlation with the observed geoid is in the spherical harmonic domain, whereas the regional correlation over North America is in the spatial domain. Dynamic topography is given by $\Delta h = \sigma_{zz}/\Delta\rho g$, where σ_{zz} is the radial component of the stress tensor, $\Delta\rho$ is the differential density between mantle and air/water and g is the acceleration due to gravity. It is the surface deflection caused by viscous stresses due to present-day mantle convection (*cf.* Braun 2010). Since it cannot be directly measured, we estimate dynamic topography by calculating the residual topography, which is the topography obtained by subtracting the isostatic component from

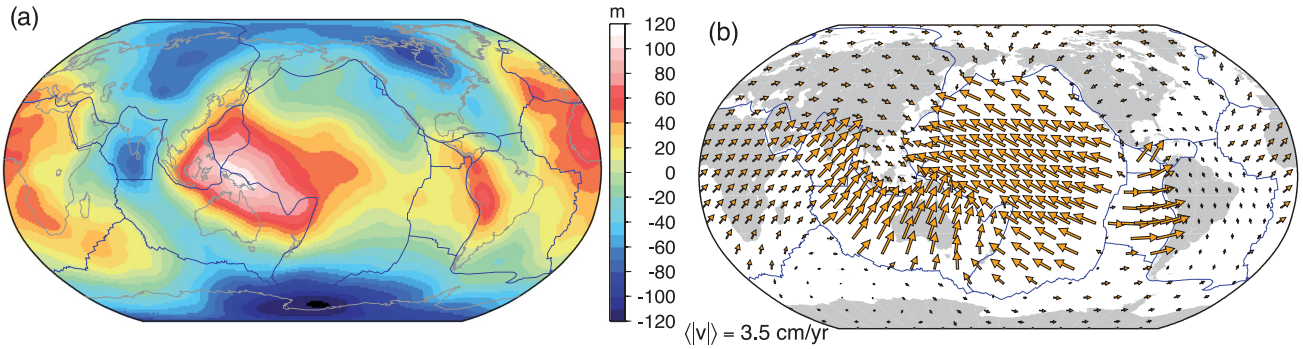

Figure 2. (a) Global geoid anomaly from Mayer-Guerr (2006), corrected for the hydrostatic shape of the Earth following Nakiboglu (1982). (b) Plate mentions from NUVEL1A in an NNR reference frame. The global rms velocity is indicated at the bottom left.

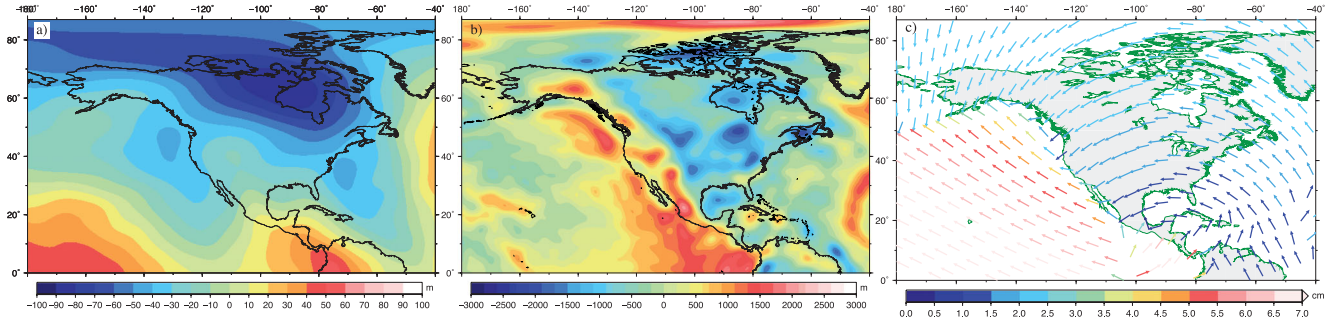

Figure 3. Observed (a) geoid, (b) estimated residual topography and (c) plate motions over North America. The velocity in (c) is indicated by the colour of the arrows.

observed topography (e.g. Forte *et al.* 1993; Panasyuk & Hager 2000; Steinberger *et al.* 2001). The underlying assumption is that all topographic anomalies not supported by our crustal density model are caused by mantle flow and are not due to static component of the lithosphere. We do not make any correction in the oceans for seafloor age dependence. The estimates of residual topography can vary with respect to each other because of uncertainties in crustal models. We calculate residual topography using the Crust2.0 model (http://igppweb.ucsd.edu/~gabi/rem.html), which we compensate (adjust the height of the lithospheric columns) at a depth of 100 km below sea level by assuming a constant pressure everywhere at that depth, calculated based on a mid-oceanic ridge column. The residual obtained by subtracting this compensated topography from the observed topography gives an estimate of dynamic topography (Fig. 3b).

For plate motions we use the NUVEL1A model (DeMets *et al.* 1994) in a no-net-rotation (NNR) frame (Figs 2b and 3c). The predicted deviatoric stress tensors are compared to the SH_{max} directions from the World Stress Map (WSM) (Heidbach *et al.* 2008), which are interpolated on our model grid. All stress estimates from WSM were used except those from the ridges, Labrador Sea (where stress observations are highly variable) and Gulf of Mexico margin (where stress observations potentially reflect gravitational sliding of the thick sediment layer).

2.1 Tomography only models

Comparison of mantle velocities predicted from the global tomography and nested models shows how flow is affected by this newly imaged density structure (Fig. 4) (e.g. Becker 2012). Overall, upwellings occur where seismic velocities are slow, and horizontal velocities converge near the bottom of the seismically slow volume and diverge near the base of the lithosphere; the opposite is true for seismically fast anomalies. A difference between pure global and nested models is also seen in the modelled dynamic topography over North America (Fig. 5).

These pure tomography models predict global and regional geoid (Figs 6a and b) that are in good agreement with the observed geoid with a correlation of 0.82 and 0.74, respectively (Figs 2a and 3a) (*cf.* Ghosh *et al.* 2010). The correlation coefficients are computed up to spherical harmonic degree $l = 20$. We see geoid highs over the subduction zones as well as prominent highs over the African and Pacific anomalies. The geoid low over the Hudson Bay is represented well. These models also predict plate motions that yield a good fit (correlation ≈ 0.85, computed up to spherical harmonic degree $l = 31$) globally with the observed global motions from NUVEL1A, both in an NNR frame (Fig. 6c). However, the amplitude of plate motions are lower than observed, and predicted velocities over North

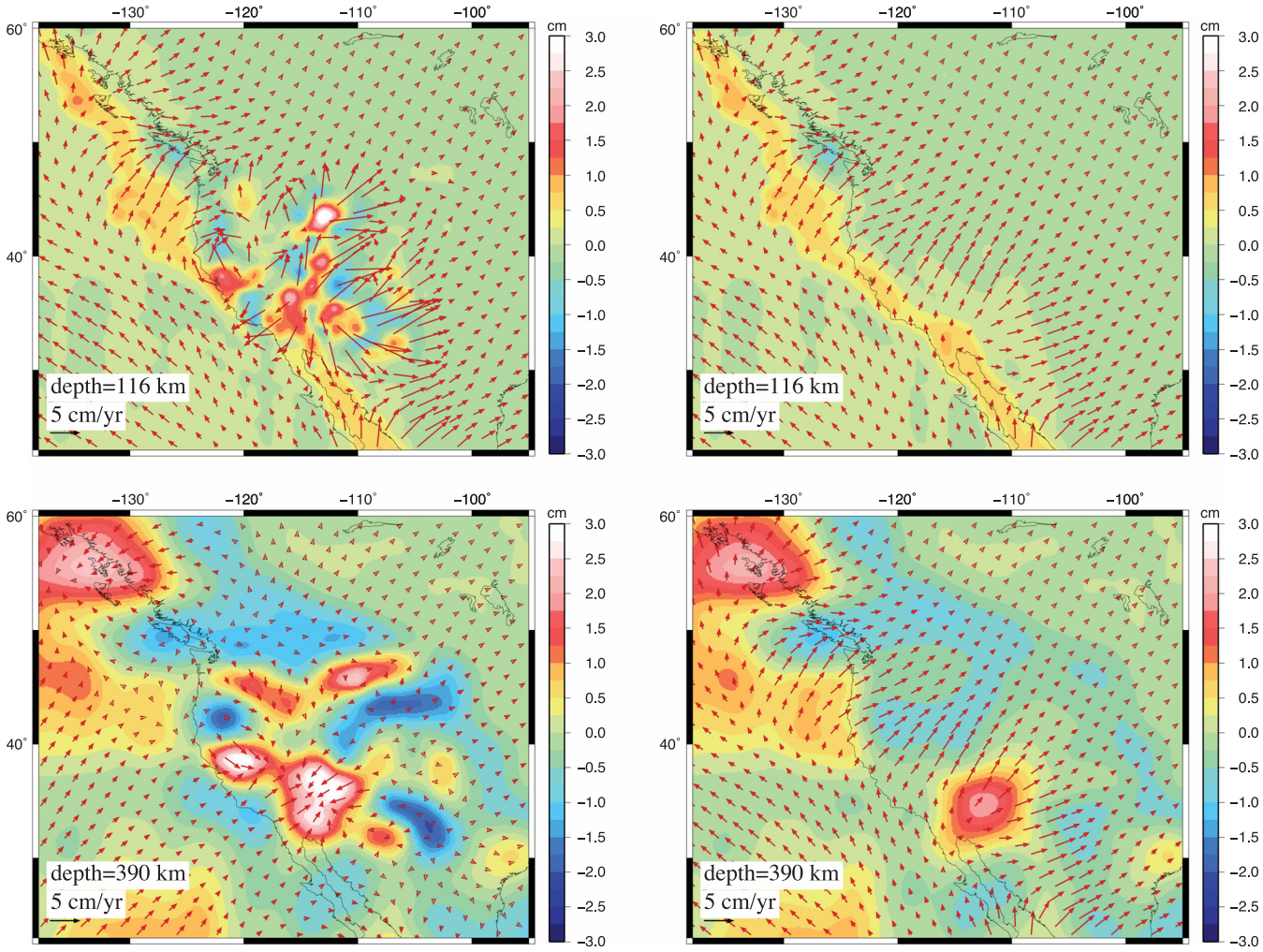

Figure 4. Horizontal velocity plotted on top of radial flow underneath western North America from nested model SH_TX2008 (left-hand side) and TX2008 (right-hand side) at two different depths. Small scale convection can be seen at shallow depths for the SH_TX2008 model. For the same model, return flow is seen at deeper depth.

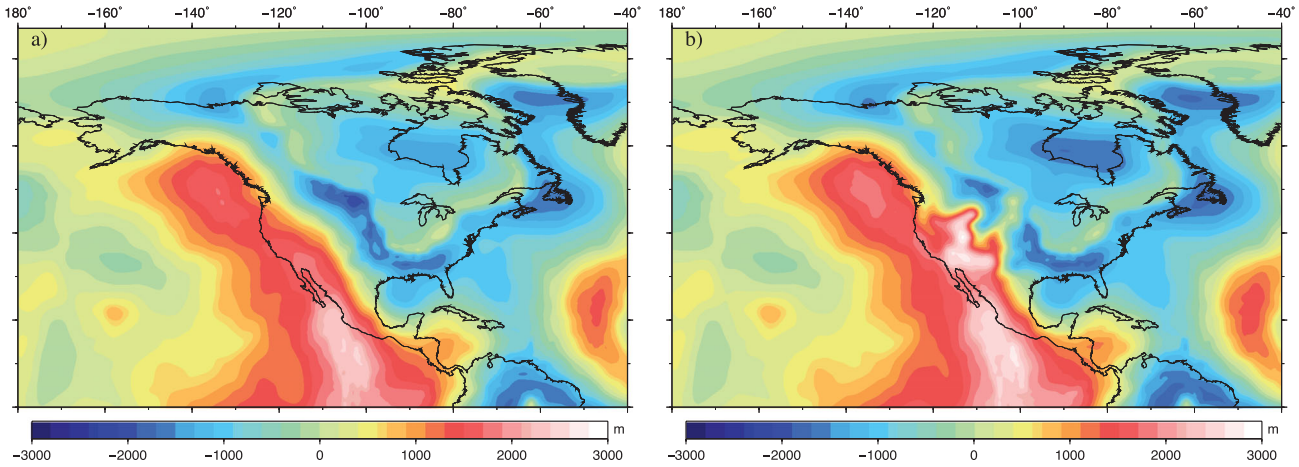

Figure 5. Dynamic topography predicted from (a) TX2008 and (b) nested model, SH_TX2008.

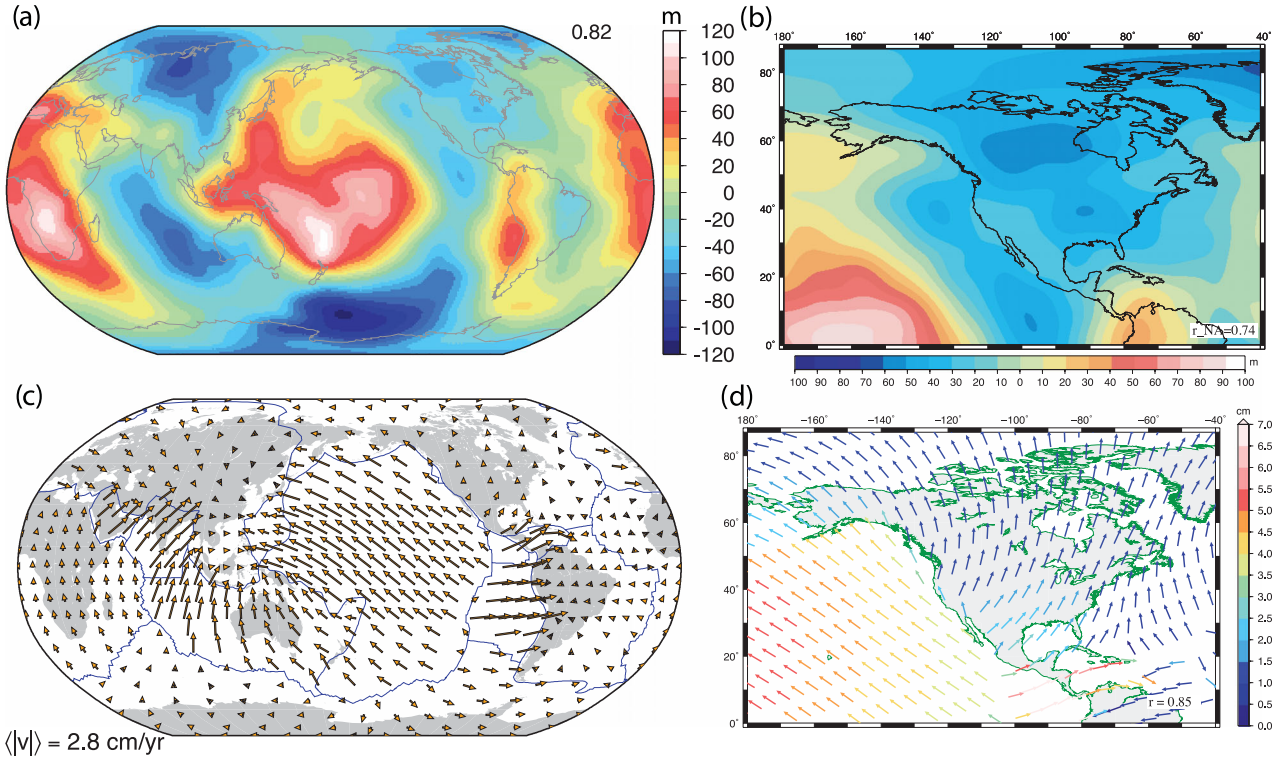

Figure 6. (a) Global geoid from tomography model SMEAN. The correlation coefficient up to degree and order 20 is noted at the top right. (b) Regional geoid over North America with regional correlation given at the bottom right. (c) Global plate motions from the same model in an NNR frame with the global rms velocity noted. (d) Velocity over North America in an NNR frame. The colour of the velocity vectors indicates magnitudes. The global correlation with NUVEL1A up to degree 31 is given at the bottom right of the figure.

America do not fit the observed motion (Fig. 6d). The fit to these constraints over North America could potentially be improved by accounting for compositional anomalies within the mantle (e.g. Forte *et al.* 2010), and which we do not attempt in this study. We keep the model simple and instead test more obvious density sources such as upper mantle slabs and GPE variations, as discussed later.

2.2 Tomography plus upper mantle slabs

While global *S*-wave models image large scale upper-mantle structure well, they typically lack the regional resolution to image slabs. Slabs appear as patches of high-velocity anomalies instead of continuous structures. Hence, we test a few cases where we include the RUM slab model in conjunction with SH_TX2008 tomography model. We keep the top 100 km from tomography as it is. Below 100 km, we replace only the high-velocity anomalies from the tomography model with the slab model, leaving the low-velocity anomalies intact (*cf.* Ghosh *et al.* 2010; Stadler *et al.* 2010; Becker & Faccenna 2011). The assumption is that all the high-velocity anomalies imaged in a tomography model are subducting slabs that are better represented in the RUM model. There is not much change in the predicted geoid or dynamic topography between the combined slab plus tomography models (Figs 7a,b) and the pure tomography models, both yielding high regional and local correlation. It should be noted that our high global correlation of dynamic topography with residual topography would be reduced if we were to remove

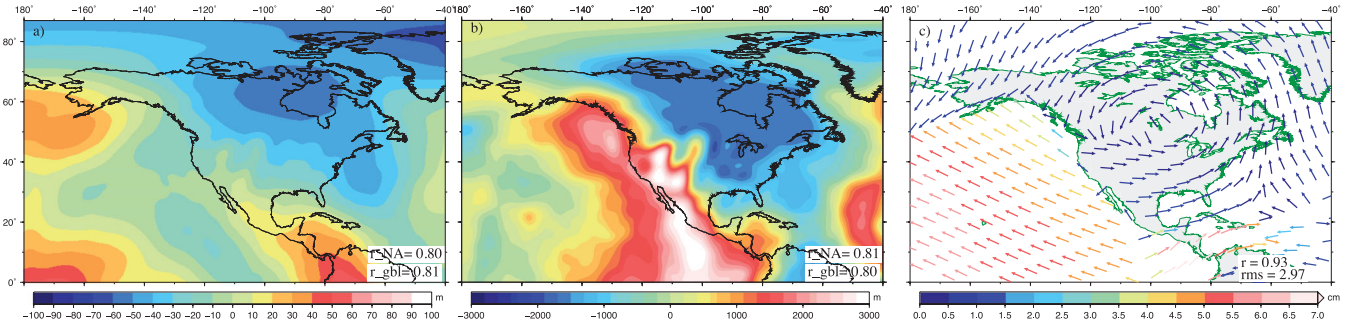

Figure 7. Predicted (a) geoid, (b) dynamic topography and (c) plate velocity over North America from the combined slab plus tomography model (RUM + SH_TX2008).

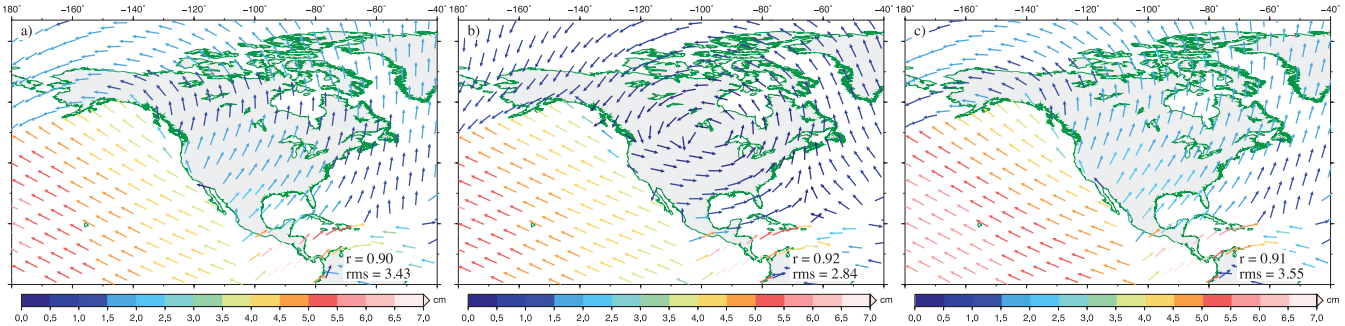

Figure 8. Predicted velocity field over North America for the slab plus tomography model (RUM + SH_TX2008) from different sources of LVVs: (a) weak zones only, (b) weak zones plus strong keels and (c) weak zones plus temperature dependent viscosity.

the seafloor age signal. However, plate motion over North America improves considerably when slabs are included (Fig. 7c). The global correlation to plate velocities also improves (0.93) and globally the plates move faster with the addition of upper-mantle slabs as shown earlier by Becker & O'Connell (2001) and Conrad & Lithgow-Bertelloni (2002). There is a rotation of velocity vectors towards the west of the North American continent, as opposed to what is observed, which is presumably due to the juxtaposition of strong lateral variations between weak plate boundary to the west and the craton to the east. We overpredict the dynamic topography, especially the positive dynamic topography over western North America. However, the model picks up the small regional lows over areas such as the Great Lakes (Fig. 7b) in contrast to Forte *et al.* (2010), who predicted a uniform slightly negative dynamic topography over much of North America. The top 200 km of density structure has the most influence on our predicted dynamic topography, as topography kernels are most sensitive to shallow structures. Henceforth, the models that are discussed use the combined models, RUM + SH_TX2008.

One of the main goals of this study is to examine the effect of LVVs on the various observational constraints. To do this, we compare models with different LVVs to see how inclusion of different LVVs affects the results. The importance of weak zones in fitting observed plate motions is well known (Ricard & Vigny 1989; King & Hager 1990; Zhong & Gurnis 1995a,b). Hence, here we examine the importance of other sources of LVVs, such as keels and temperature dependent viscosity in matching the observational constraints over North America. The geoid and dynamic topography globally and over North America are not affected to a large extent by these different sources of LVVs unlike plate velocities, which are sensitive to these laterally variable viscosity sources (Becker 2006; Ghosh *et al.* 2010; van Summeren *et al.* 2012). Hence, we restrict our discussion to plate motions. We take the RUM + SH_TX2008 density model discussed above and remove all other sources of LVVs except those from weak zones. The resultant velocity shows a N–S orientation over North America with a slight decrease in global correlation and an increase in overall plate speeds (Fig. 8a). We next introduce strong keels (100 times stronger than the ambient lithosphere and mantle) in the upper 300 km in addition to the weak zones. The velocity over the North American plate (Fig. 8b) resembles the case with all sources of LVVs included (Fig. 7c), although the plate slows down slightly, as is also evident from the global rms velocity reduction. Finally, we examine a case where we add temperature dependent viscosities in the mantle below 100 km depth in addition to the weak zones. The direction of the velocity field is similar to that of the case with weak zones alone (Fig. 8a) with the North American Plate moving slightly faster and a slight global increase in rms velocity (Fig. 8c). The above results indicate that although the global fit to plate motions remains almost the same, irrespective of whether we take into account strong keels or temperature dependent viscosity, the presence of the strong cratonic root helps to move the North American Plate in a more westerly direction, as is observed, compared to a case where weak zones are considered alone. Including temperature dependent viscosity does not affect the orientation of plate motion, however, it helps to speed up the plate slightly. Considering all three LVVs, weak zones, strong keels and temperature dependent viscosity gives the best fit in terms of direction and velocity amplitude.

3 EFFECTS OF TOPOGRAPHY AND SHALLOW LITHOSPHERE STRUCTURE

Topography and shallow lithospheric buoyancies give rise to GPE differences that can constitute an important component in global force balance. Earlier studies (Bird 1998; Steinberger *et al.* 2001; Lithgow-Bertelloni & Guynn 2004; Bird *et al.* 2008; Ghosh *et al.* 2008; Naliboff *et al.* 2009; Ghosh & Holt 2012; Ghosh *et al.* 2013)

have investigated the combined effects of these GPE variations in addition to mantle tractions on global lithospheric stress by treating the two components separately. Here, we have developed a new way of incorporating GPE variations directly in our global circulation models. We do so by applying the GPE gradients as a stress boundary condition. The gradient in potential energy per unit area, (∇U) can be related to basal tractions ($\sigma_{r\theta,\,r\phi}$) by $\sigma_{r\theta,\,r\phi} \approx -\frac{L_0}{L}\nabla_{\theta,\,\phi}U$ (Fleitout & Froidevoux 1983), where L is the isostatic compensation depth, L_0 is the lithospheric thickness and $\nabla_{\theta,\,\phi}$ are the θ and ϕ components of the horizontal gradient operator.

We first calculate gradients of GPE from the CRUST2.0 model. Since Crust2.0 is uncompensated, we compensate the model at a reference level of 100 km below sea level by assuming a constant pressure at that depth and adjusting the density of the subcrustal layer (Ghosh *et al.* 2009). The observed topography is a combination of both static and dynamic parts. The effect of dynamic topography, caused by radial flow, is already included in the mantle circulation model. Hence, if we do not compensate the crustal model, we would in essence count the effect of radial tractions twice. The GPE gradients are then converted to shear tractions ($\sigma_{r\theta,\,r\phi}$) that are applied as boundary condition at the surface down to a depth of 50 km. Our benchmarking tests show that this method of applying GPE as stress boundary condition in the circulation models gives accurate stress estimates in the test cases which are constructed by our prior approach of computing the contributions separately with thin shell models (see Appendix).

4 STRESS FIELD

In this section we discuss the stress response of the models to mantle tractions and GPE variations individually, as well as to the combined effect of GPE variations and mantle flow. We evaluate the deviatoric stress field over North America from our best fitting density (RUM + SH_TX2008) and viscosity models. We determine the most compressive principal stress axes and perform a quantitative comparison of these stress axes with the $SH_{\max}$ directions of the WSM by computing both angular misfit and regime misfit. The angular misfit (θ) is simply the difference in the $SH_{\max}$ directions between our model prediction and the WSM and it ranges from 0° to 90°. As for the regime misfit (R) the $SH_{\max}$ stress axes are assigned values between 1 and 3 depending on whether they are tensional, compressional or strike-slip. A difference in the regimes will range from 0 for the same style of stresses to 2, where the style is completely opposite. Next, we compute a total misfit, which is a joint indicator of both the angular and regime misfit, by calculating $\sin\theta \times (1 + R)$. The total misfit lies between 0 and 3, where a low score indicates a good fit to the WSM observations and a high score indicates a poor fit.

The deviatoric stress field arising from mantle tractions alone in the Great Plains and Rocky Mountains is dominated by an ENE–WSW compression, which changes into pure extension farther west in the Snake River Plain, western part of Colorado Plateau and Basin and Range (Figs 9a and 10a). The Colorado Plateau shows dominant strike-slip style of deformation in the eastern part as opposed to observed E–W extension, which transforms into NW–SE extension in the western part of the plateau, as observed. The Sierra Nevada also shows a strike-slip regime, whereas the Cascades exhibit dominant NE–SW compression. The Basin and Range shows extension in the eastern part and strike-slip faulting in the west. The predicted most compressive principal stress axes show a very good match with the WSM $SH_{\max}$ directions in the northern part of Great Plains region in both style and orientation. However, within the Great Plains and in the Rockies, our models predict too much ENE–WSW compression whereas the WSM stresses show ENE–WSW extension. In fact, in the central and southern Rockies, there is a complete mismatch of the modelled and observed stresses (Fig. 11a). We also match the WSM $SH_{\max}$ directions in most of the Basin and Range, although there is a mismatch of style in the western part of the Basin and Range. We predict strike-slip in Yellowstone as opposed to observed tensional stresses there. The Snake River Plain shows a moderate fit, with our model predicting the correct style, but being offset by $\sim$25–30°. The Columbia Plateau also shows a good fit. A quantitative assessment of the goodness of fit between our predicted $SH_{\max}$ and those from WSM shows a total misfit of 0.69. The worst fit is in the central and southern Rocky Mountain area. The average stress magnitude ranges between 30–40 MPa (Fig. 10a).

4.1 Stresses from GPE differences

Since many studies have emphasized the importance of GPE in affecting the deformation of the western United States, in this section we examine the effect of GPE alone on the deviatoric stress field in that region. In this case, the lithospheric stress is created by surface tractions from GPE gradients; no mantle density anomalies are considered. The deviatoric stresses predicted from GPE dominate in the regions west of the Great Plains (15–20 MPa), where they are tensional (Figs 9b and 10b), whereas east of the Great Plains the average stress magnitude is $\sim$10 MPa and are compressional. In the Rockies, the Snake River Plain and the Colorado Plateau, the $SH_{\max}$ orientation and tectonic style are in almost perfect match with the WSM stress axes for this case (Fig. 11b). However, in the Sierra Nevada, Great Valley and Columbia Basin, GPE alone predicts too much extension. In the southern Basin and Range, the density driven tractions fare better in fitting the $SH_{\max}$ orientations. Also, north of the Columbia Plateau, the GPE only case fails to match observed orientation and style of the WSM stress axes. Hence, in many parts, especially toward the eastern part of western United States, stresses from GPE variations fit the WSM stresses considerably better than those from mantle tractions alone, at least in terms of style of deformation. However, in areas such as the Cascades, Columbia Plateau, Sierra Nevada, south of Colorado Plateau, mantle tractions fit the WSM stresses better than those from GPE variations (Fig. 11b). In order to investigate whether the stresses from GPE owe their origin to oceanic variations (ridge-push) versus continental variations (*cf.* Becker & O'Connell 2001), we compute stresses from a separate model where the GPE related tractions are applied only in the oceanic areas. In the western United States, there is a clear dominance of continental GPE variations (Fig. 12) as compared to ridge-push only. It should be noted that the accuracy of GPE calculations are limited to the accuracy of the crustal model (Crust2.0). Improved crustal models can potentially improve the fit to observations.

4.2 The composite model: mantle tractions plus GPE response

The deviatoric stresses from the combined model introduces a stronger tensional component in the Basin and Range, Colorado Plateau as well as parts of central and southern Rockies (Figs 9c and 10c), as is observed. The strike-slip deformation in the eastern part of the Colorado plateau from mantle tractions alone (Fig. 9a) improves to become NW–SE extension. The western part of the Basin and Range is more extensional than the case with mantle tractions

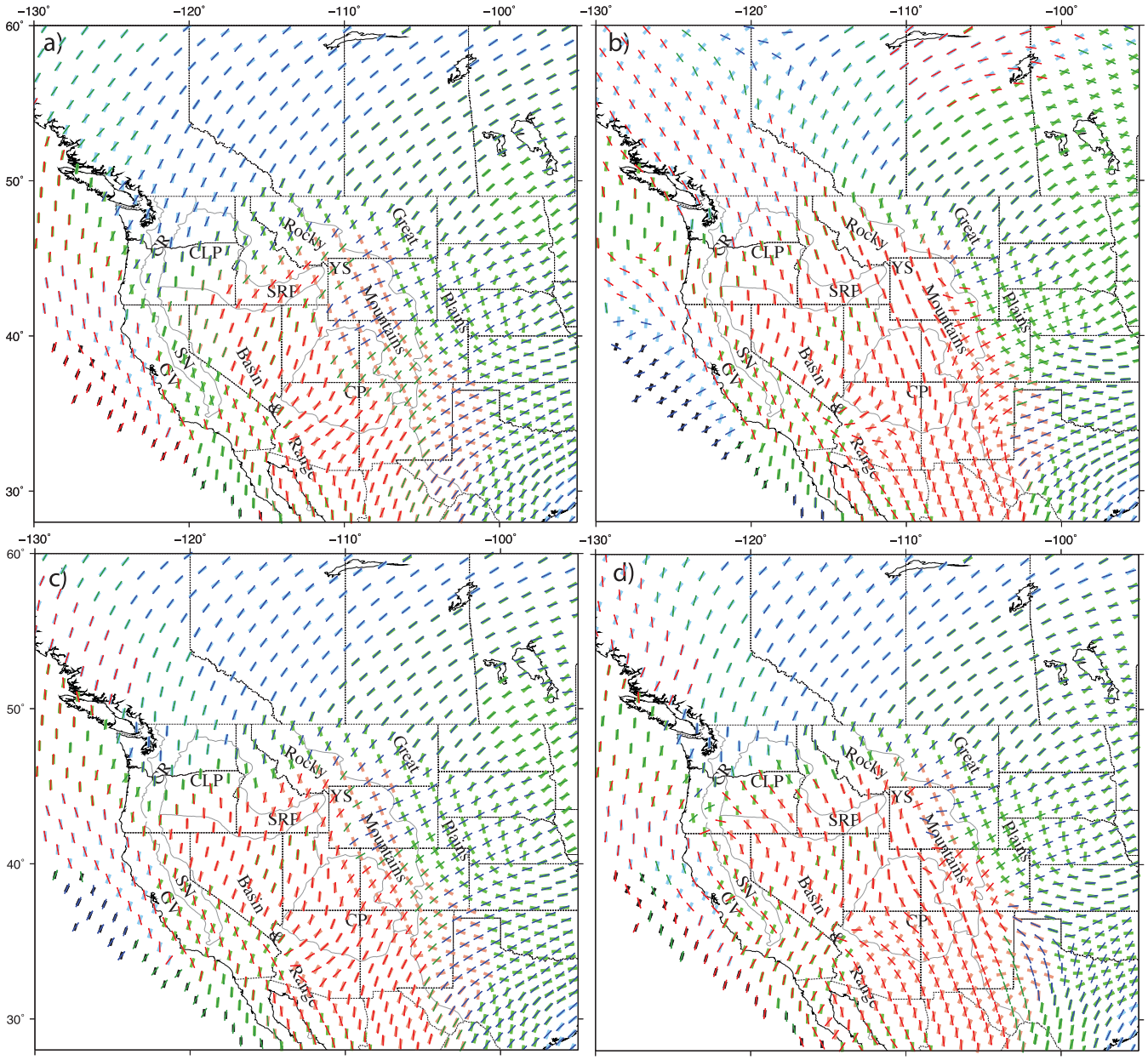

Figure 9. The most compressive principal stress axes plotted on WSM SH_{max} directions (thick axes). Red indicates extensional regime, blue indicates compression while green denotes strike-slip. The grey line delineates the different tectonic regions in western United States: CP, Colorado Plateau; SN, Sierra Nevada; SRP, Snake River Plain; GV, Great Valley; CR, Cascade Ranges; CLP, Columbia Plateau; YS, Yellowstone. The four cases represent (a) model with mantle density anomalies only, (b) model with effect of GPE only, (c) combined model driven by both mantle density anomalies as well as GPE differences and (d) same as in (c), but with the addition of anistropic viscosity along the San Andreas fault.

only. The stresses match those in WSM in the Columbia Plateau and the Snake River Plain in both orientation and style. There is still a large mismatch between predicted and WSM stresses in the central and southern Rockies as well as southern part of the Great Plains mainly due to the compression from the east, although the misfitting area is smaller than before (Fig. 11c). The total misfit reduces to 0.62 with the introduction of GPE, which is lower than both the mantle only and GPE only case. The stress magnitudes increase in the western part with an average between 30–40 MPa (Fig. 10c), consistent with those modeled by Humphreys & Coblentz (2007) and Ghosh *et al.* (2013).

The main problem area is the central and southern Rockies and the western Great Plains that fail to match the WSM stress field (Figs 9 and 11). The rotation of stress axes from NE–SW to NW–SE occurs farther west in our model compared to what is observed (*cf.* Zoback & Zoback 1980, 1981). Humphreys & Coblentz (2007) discussed the importance of GPE variations in the stress effect of the western United States. They also concluded that high coupling between the lithosphere and the mantle occurs only below the craton and west of the craton coupling is small. However, models with a weaker asthenosphere (low coupling) do not resolve the problem of the NE–SW compression in the Rockies. In fact, our results indicate that a weak coupling (minor effect of mantle tractions) is required beneath the Rockies, the eastern part of the Colorado Plateau and the western Great Plains, where GPE alone does an excellent job of fitting the observed stresses. In the rest of the western United

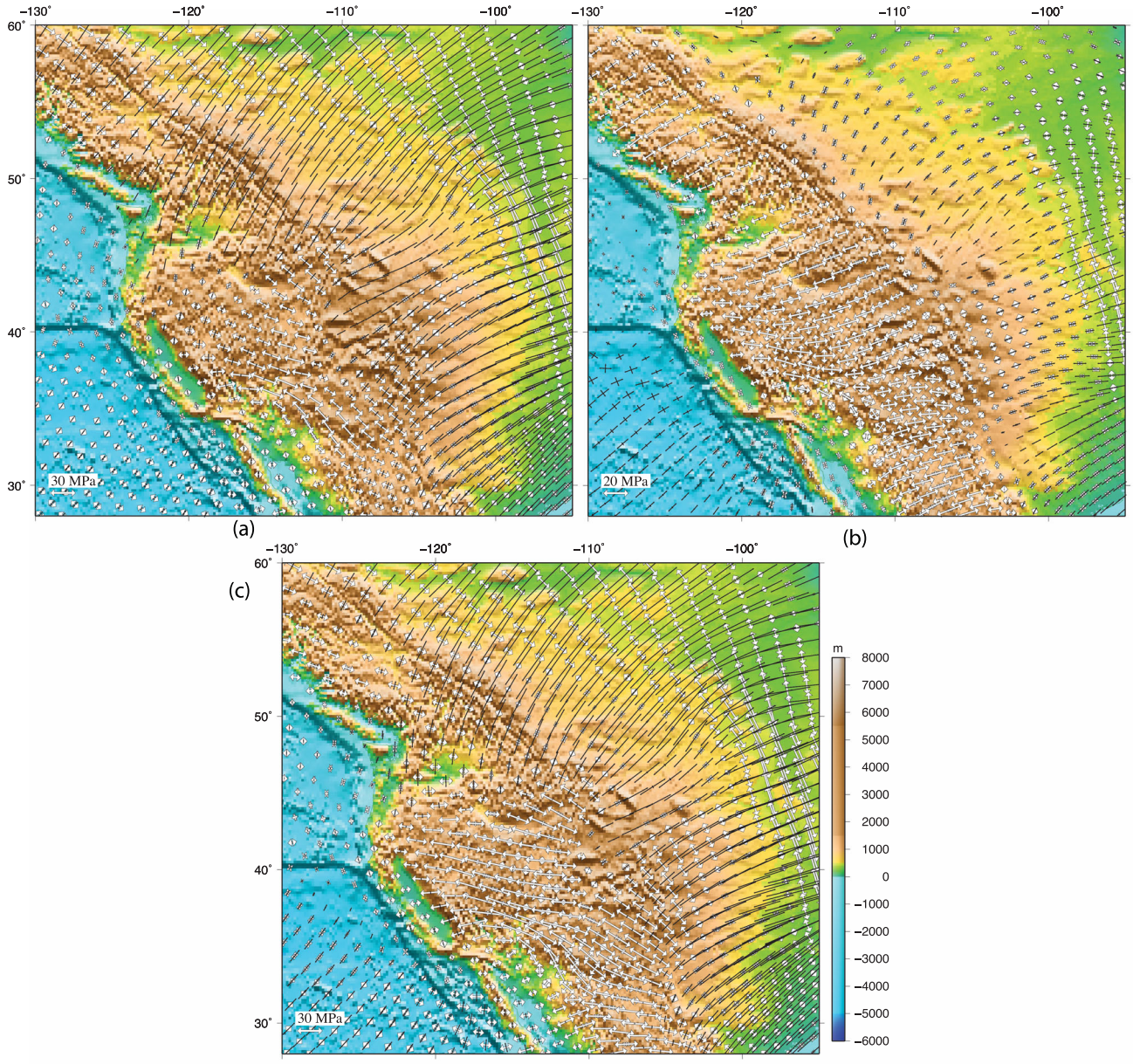

Figure 10. Horizontal deviatoric stresses predicted from (a) model with mantle density anomalies only, (b) model with GPE variations only, (c) combined model driven by both mantle density anomalies as well as GPE differences, plotted on top of ETOPO1 topography. The black axes indicate compression whereas the white axes denote tensional stresses. Strike-slip regime is denoted by a pair of black and white axes. Note the smaller scale for the GPE stresses in (b).

States, a combined GPE plus mantle traction model fares better in fitting the WSM stresses, indicating a stronger coupling.

When the effect of GPE variations is considered, the velocity of the North American and the Pacific plates increase, while the direction of North America and Pacific are more or less the same (compare Figs 7c and 13c). The global rms velocity is 3.49, which is very close to the observed global rms velocity of 3.5. The global fit to plate motions is excellent with a correlation coefficient of 0.91. The regional geoid over the continent gives a correlation of 0.77, with a deeper trough over Hudson Bay than the mantle traction only case, whereas the global geoid fit is slightly better (correlation 0.82) as shown in Fig. 13(a). The observed geoid over North America shows a prominent low over Hudson Bay (80–90 m) which is larger in amplitude than the predicted geoid (60–70 m). The pattern of dynamic topography fits the residual topography well both over North America as well as globally ($r > 0.80$), (Fig. 13b) (*cf.* Steinberger *et al.* 2001; Forte 2007). However, as before, we overshoot the amplitude of the dynamic topography by a few hundred metres. The rotation of velocity vectors towards the west of North America persists.

4.3 Effect of a slightly stronger San Andreas Fault

In the above models, the SAF has the same strength as the weak zones in the other parts of the models. We experiment with various strengths of the SAF, where we make the SAF both weaker and stronger than the weak zones elsewhere. We present the results of the case, which best fits the various observational constraints. We take our combined best fitting model from the previous section and assign the San Andreas fault to be ∼10 times stronger than the other weak zones. The direction of plate motion over North America

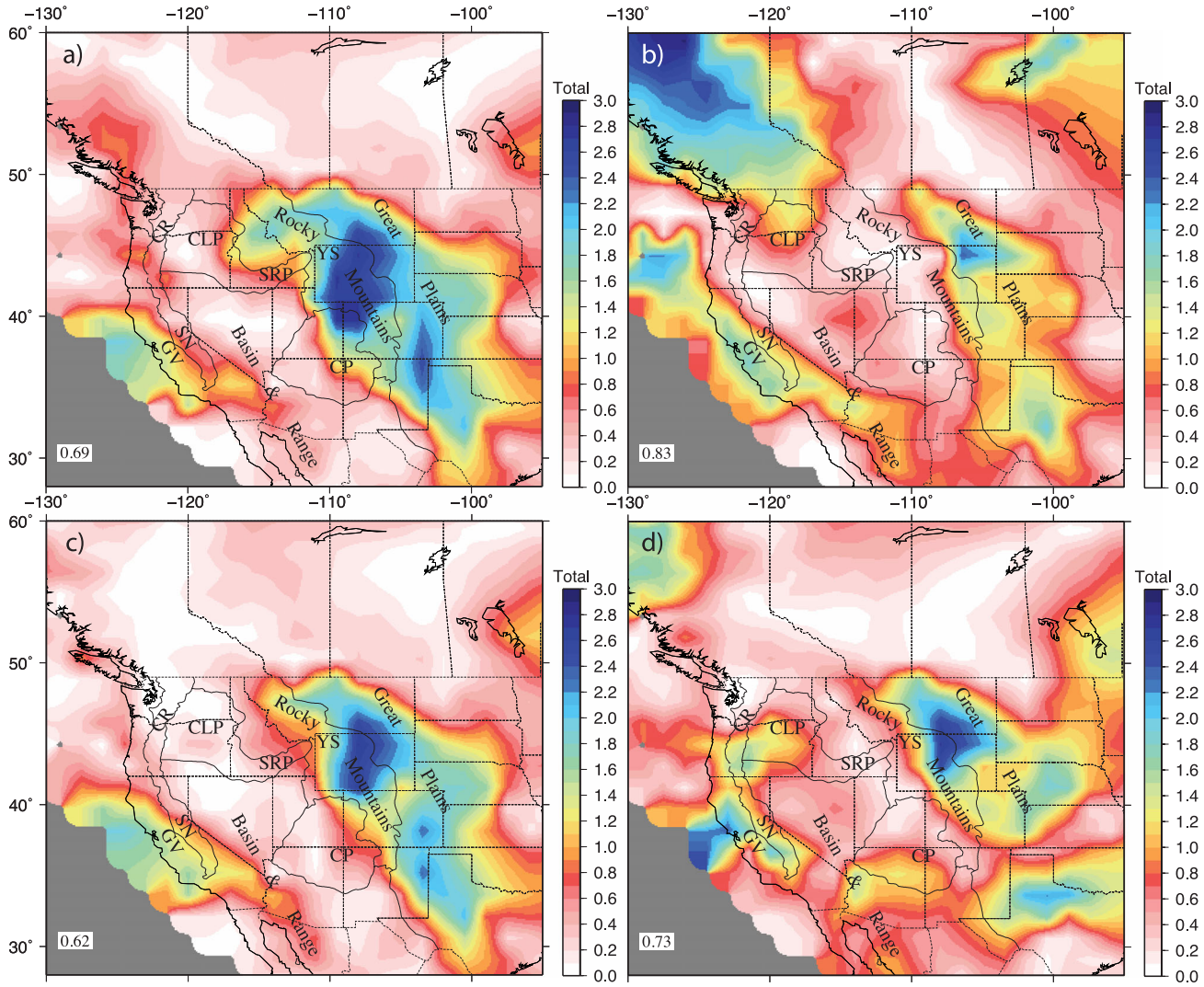

Figure 11. Total misfit between the observed (WSM) SH_{max} directions and predicted SH_{max} directions from (a) model with mantle density anomalies only, (b) model with GPE variations only, (c) combined model with both mantle density anomalies as well as GPE variations, (d) same as in (c), but with the addition of anistropic viscosity along the San Andreas fault.

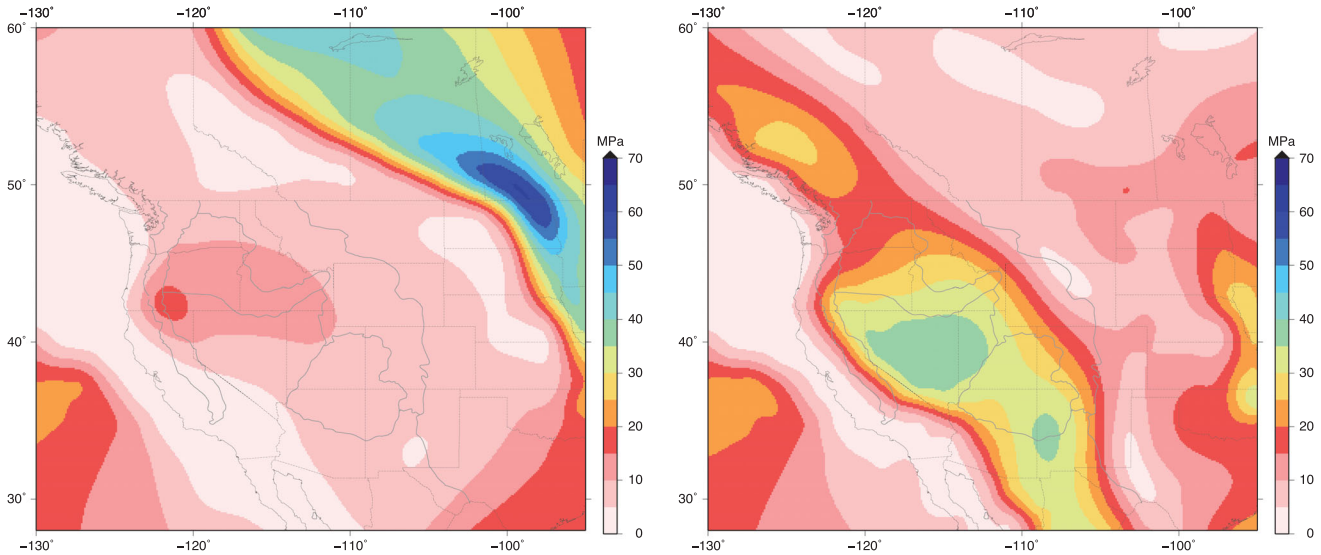

Figure 12. Second invariant of deviatoric stress magnitudes from GPE variations in oceanic areas only (left-hand side) and globally (right-hand side). In western United States, the continental GPE variations play a dominant role as compared to oceanic GPE (ridge-push).

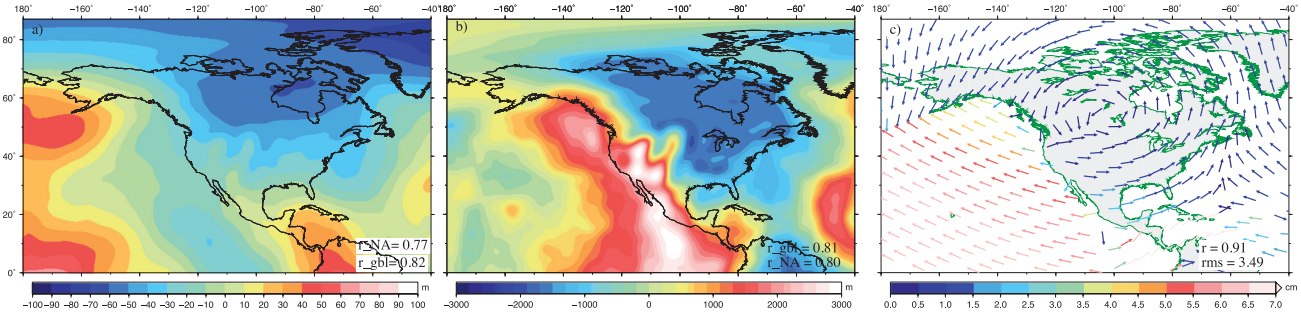

Figure 13. Predicted (a) geoid, (b) dynamic topography and (c) plate motion over North America from combined model driven by density anomalies in the mantle as well as GPE differences.

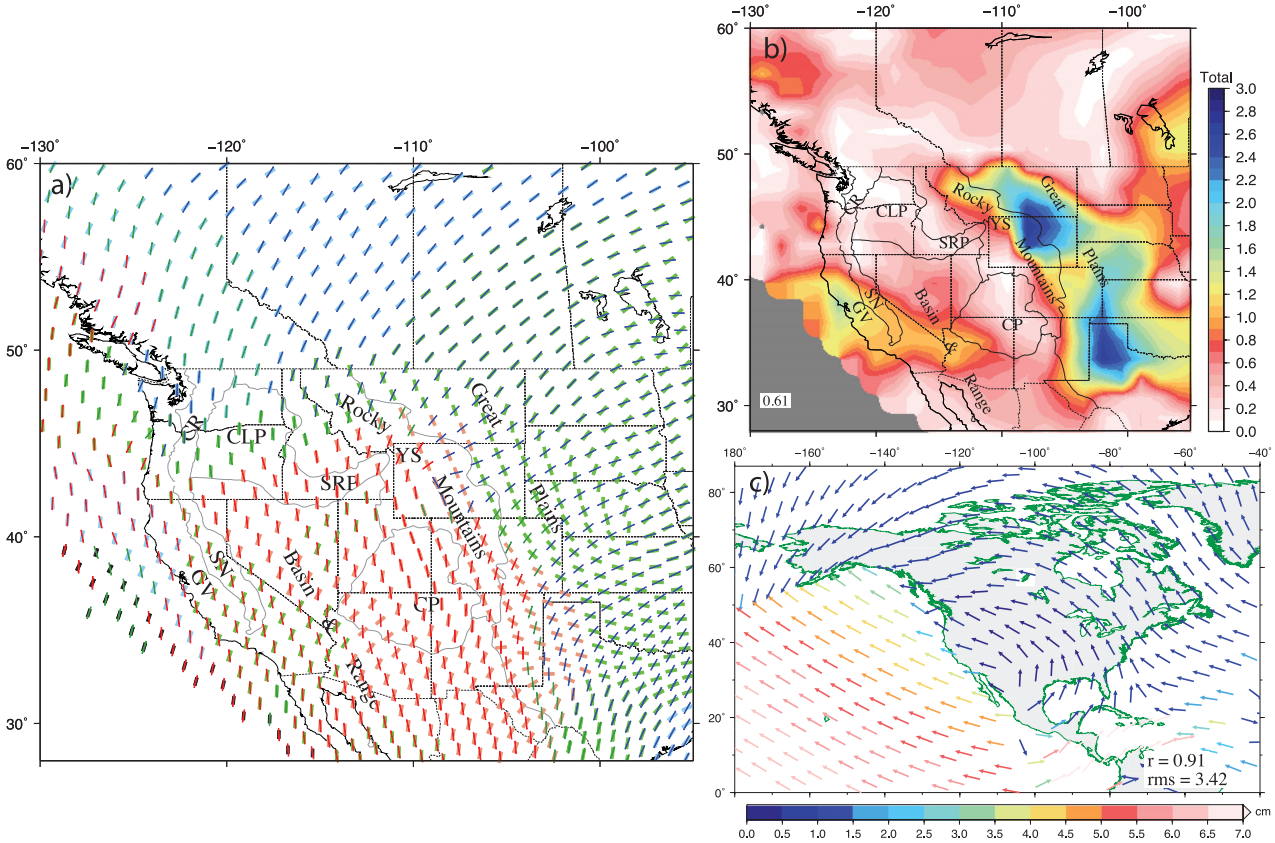

Figure 14. Prediction from a case where the SAF is assigned a slightly higher viscosity than the weak zones in the other parts of the world. (a) Most compressive principal stress axes plotted on WSM SH_{max} axes, (b) Total misfit between the predicted and WSM SH_{max} axes, (c) predicted velocity over North America.

improves and the rotation of velocity vectors to the west of the continent, seen in the previous case, is no longer present (Fig. 14c). The fit to the stresses also improves with the overall misfit being slightly lower (Fig. 14a,b). The assumption that the San Andreas fault is slightly stronger compared to the segments to the north and south, where there are triple junctions, had been proposed by Platt *et al.* (2008). They argued that this difference in strength along the fault serves to explain second order compression and extension features distributed antisymmetrically around the fault.

5 EFFECT OF ANISOTROPIC VISCOSITY

Previous studies (e.g. Gilbert & Scholz 1994; Zoback 2000; Jackson 2002) have argued that the stress near the San Andreas fault is influenced by the fact that it is weaker along the direction of shear. The effect of this directional dependence of viscosity on global mantle flow and regional lithospheric stress remains an open question. Christensen (1987) has shown through 2-D experiments that anisotropic viscosity can affect post-glacial rebound and geoid. Han & Wahr (1997) also examined post-glacial rebound in response to anisotropic viscosity. Lev & Hager (2008, 2011) found that Rayleigh–Taylor instabilities are considerably affected by presence of anisotropic viscosity. Becker & Kawakatsu (2011) examined the role of anisotropic viscosity on plate scale flow in global 2-D and 3-D models and concluded that significant trade-off between isotropic and anisotropic viscosity variations could make it difficult to distinguish the two effects from each other. We test the effect of an anisotropic San Andreas on the geodynamic response over North America.

For the implementation of the anisotropic tensor, we have taken a fully 3-D approach (*cf.* Pouilloux *et al.* 2007). We can prescribe

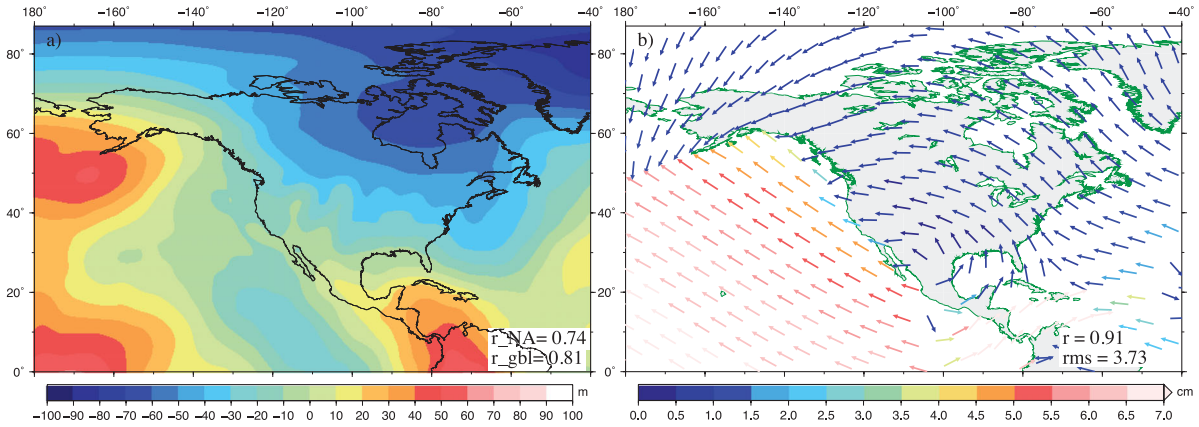

Figure 15. Predicted (a) geoid and (b) velocity from a model with LVVs along with GPE variations and with the addition of anisotropic viscosity along the SAF.

any arbitrary anisotropic tensor. However, since there is no tight constraint on the nature of anisotropic viscosity in faults, we implement a transversely isotropic (hexagonal) representation (e.g. Han & Wahr 1997) and further simplify it to a weak and strong direction. We introduce a parameter Γ, which denotes the relative variation of shear and normal viscosity. For simplicity, we set Γ to 0 (see Becker & Kawakatsu 2011). Since these models are instantaneous, they do not address the issue of how mechanical anisotropy might have arisen. We test different degrees of anisotropy of the shear plane of the San Andreas, where shear in the plane of the fault is 1, 2 or 3 orders of magnitude weaker than the normal plane. We adjust the isotropic viscosity of the fault according to the degree of anisotropy, where isotropic viscosity is inversely proportional to the square root of anisotropic viscosity, so that the net viscosity of the shear zone remains the same as the other weak zones in our model. Here, we present the results for an extreme case, where the fault is 1000 times weaker in the direction of shear. In order to accommodate this weakness, the isotropic viscosity in that particular shear zone is only 0.3 times smaller than the lithosphere, whereas the weak zones everywhere else on the planet is 100 times weaker than the lithosphere. We present a case where anisotropic SAF is taken into account in our best-fitting circulation model with LVVs and with the inclusion of GPE variations. As a consequence, the geoid over North America shows a broader trough over the Hudson Bay (Fig. 15a) as compared to the corresponding isotropic case (Fig. 13a). The rms velocity increases slightly to 3.7. The velocity field over the continent is smoother and the continent moves E–W as is observed (Fig. 15b) and the rotation of vectors no longer persists. The stress field in the western United States shows greater misfit in Colorado Plateau, Columbia Plateau as well as in the Sierra Nevadas (Fig. 11d). The effects of weaker anisotropic viscosity is similar but smaller as compared to the above results.

6 DISCUSSION AND CONCLUSIONS

We have modelled the plate dynamic forces globally with a focus on the western United States. This modelling includes a broad range of geodynamic processes; most notably a thorough consideration of LVVs and their geodynamic effects are measured against all the major observable fields (plate motion, geoid, lithospheric stress and dynamic topography). In a global sense, models that fit well all the observable fields are similar to some other global models (e.g. Steinberger *et al.* 2001; Ghosh & Holt 2012; Ghosh *et al.* 2013). The inclusion of cratonic roots and low-strength plate boundaries improves the fit to mostly geoid and plate motions. In North America, GPE is a dominant force acting in parts of western North America, especially in the Yellowstone area, the Rocky mountains and parts of Great Plains. We find that GPE is dominant in the eastern part of western United States, closer to the keel, with mantle tractions playing little or no role there. Farther to the west and north, both GPE variations and tractions play an important role and in southern Sierra Nevada, mantle tractions alone dominate. A universal reduction of the mantle contribution in western United States will not solve this problem. Shallow and deeper forces seem to act unequally over western North America with one dominating over another in different regions. One reason could be the fact that the slow and fast velocities that are imaged below western United States are not solely due to temperature variations. Many of those anomalies could be compositional or have a melt and/or water component (Schmandt & Humphreys 2010), factors which we did not explore in our study besides correcting for cratonic keels. Our model does not fit the observed stresses in parts of Rocky Mountains and Great Plains. A potential source of some of that misfit could be the isotropic nature of the stress field (both tensional and compressional axes are of equal magnitude) in some of those areas (Fig. 10c), which would be sensitive to minor perturbations. In parts of California, where strong and distinct strike-slip WSM observations exist, it may be difficult to account for stress details due to reasons such as a weak creeping San Andreas or other lithological strength contrasts. The small scale of these processes are beyond our modelling capabilities. The most compressive principal stress axes predicted globally from our best model are in accordance with the global SH_{max} directions from the WSM (Fig. 16) as well as with those from Ghosh & Holt (2012) and Steinberger *et al.* (2001). The average global angular misfit between SH_{max} directions of our best model and WSM is ∼32°, which is lower than the global azimuthal misfit that Steinberger *et al.* (2001) obtained with their free slip models and slightly higher than their no-slip models. The regime misfit of our best model is 0.68.

Other important findings are that inclusion of upper-mantle slabs in our convection models improves the plate motion of North America, potentially due to the slab beneath the Aleutian arc, and that LVVs do play a major role in affecting the dynamic observations over North America. We also examine the effect of an anisotropic San Andreas fault, finding that our modelling is not sensitive to this, presumably because these isotropic weak zones behave mechanically similar to anisotropic weak zones in shear. We additionally find that a slightly stronger SAF system best fits the dynamic

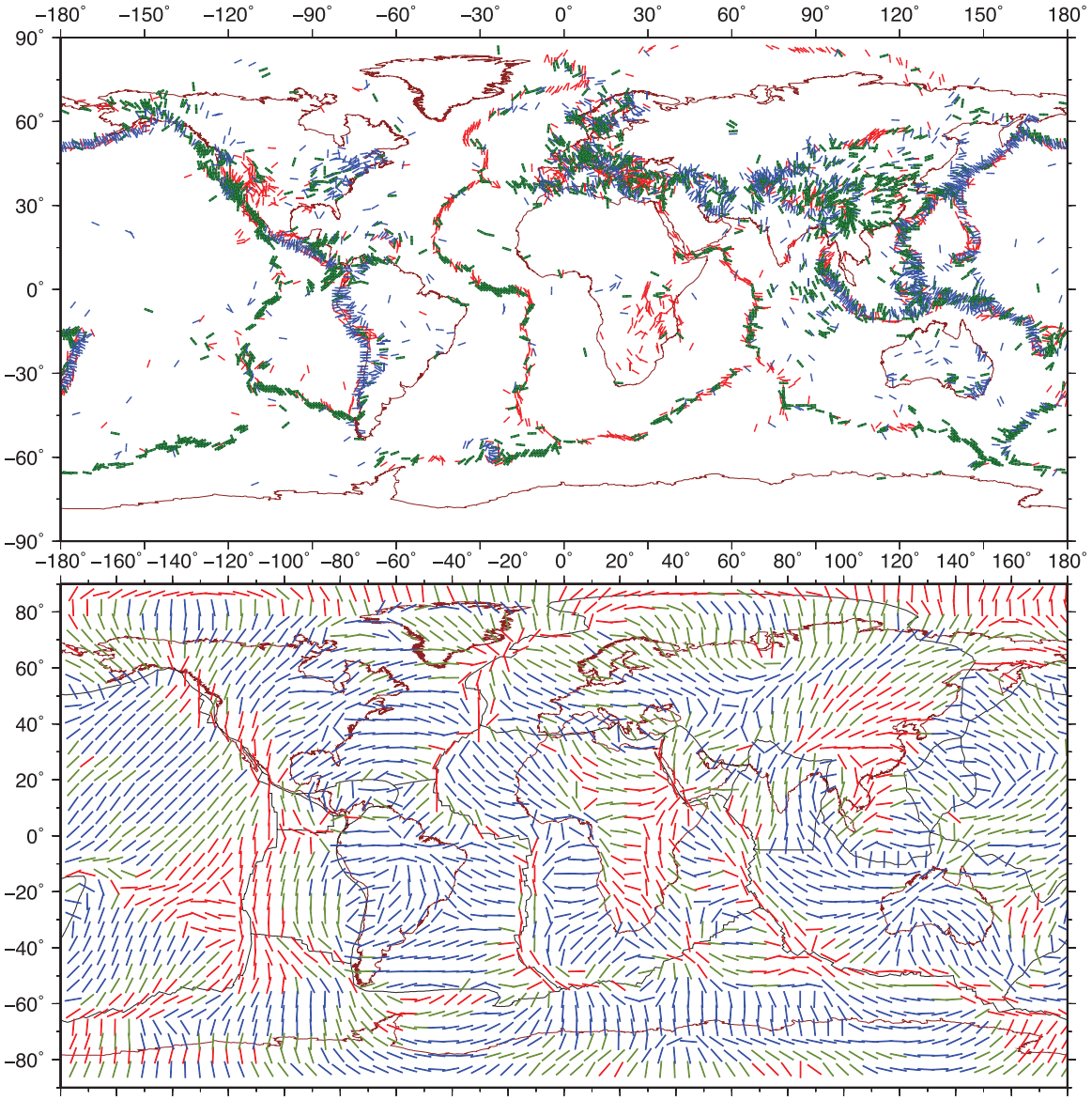

Figure 16. (top) SH_{max} directions from the World Stress Map averaged within 1° × 1° areas (e.g. Ghosh & Holt 2012). Red indicates normal faulting, blue indicates thrust faulting and green denotes a strike-slip fault environment. (bottom) Most compressive principal deviatoric stress axes from our best-fitting dynamic model.

Table 1. Quantitative comparison between different models. The correlations coefficients (r) are with respect to the observed geoid, dynamic topography and plate motions.

Models	Geoid (r)		Dynamic topo (r)		Plate Motions		Stress
	Global	Regional	Global	Regional	r	RMS (cm yr^{-1})	Misfit
Mantle tractions only	0.81	0.80	0.80	0.81	0.93	2.97	0.69
GPE variations only	0.43	0.15	—	—	0.61	0.74	0.83
Combined	0.82	0.77	0.81	0.80	0.91	3.49	0.62
Combined + anisotropic SAF	0.81	0.74	0.81	0.80	0.91	3.73	0.73
Combined + strong SAF	0.81	0.75	0.81	0.80	0.91	3.42	0.61

observations over the continent. In particular, we find that a combined model with mantle tractions, GPE variations and a stronger SAF provides a better fit to the North American plate motion and the WSM SH_{max} axes in western United States (Table 1).

Our models show that eastern North America is dominated by convergent flow, most likely due to the Farallon slab, whereas divergent flow is seen in the western part (Fig. 17). The average traction magnitude beneath the craton is ∼1.2 MPa, consistent with Ghosh *et al.* (2013), whereas it is half that value in the rest of the continent. This indicates that the coupling beneath the craton is twice that of the rest of North America. The basal tractions tend to compress North America and hold it together; GPE in the western United States overcomes this compressive force. The total basal load is about 50 × 10^{18} N, which compares to about 80 × 10^{18} N for

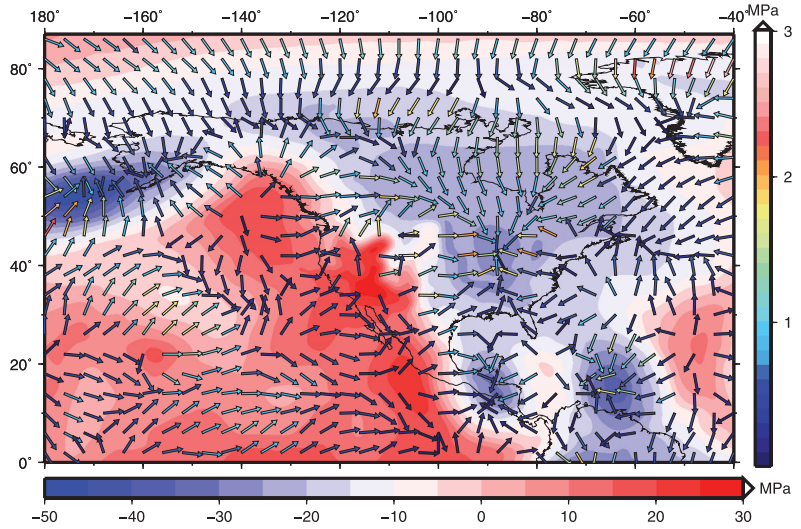

Figure 17. Horizontal tractions (side scale bar) plotted on top of radial tractions (bottom scale bar), predicted from mantle circulation at a depth of ∼120 km below North America.

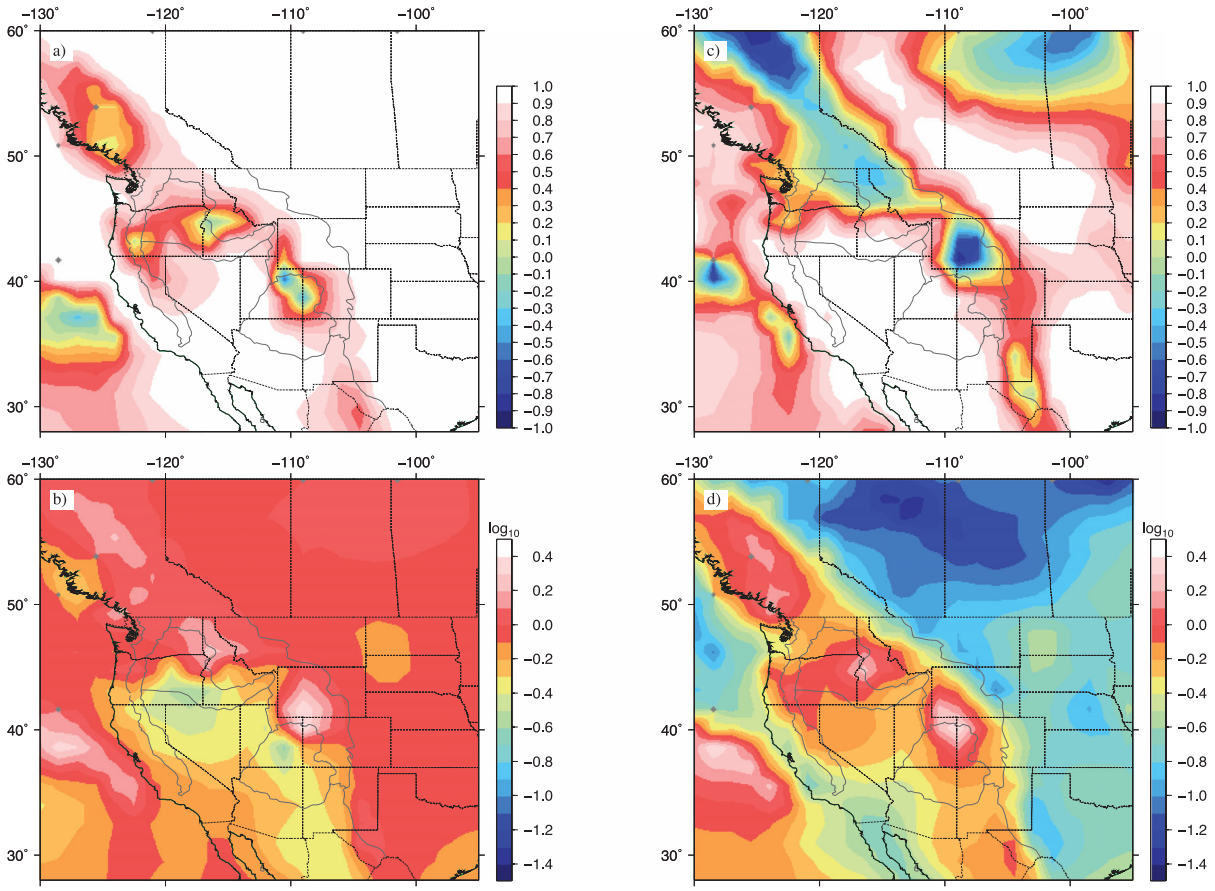

Figure 18. Comparison of the predicted deviatoric stresses between mantle only, GPE only and the combined cases. The top panel shows the correlation coefficients (r) of the deviatoric stress tensors between (a) mantle only and combined cases, (c) GPE only and combined cases. A correlation of 1 will imply that there is an exact match in direction and style. The bottom panel shows the ratio of the second invariant of deviatoric stresses (T_1/T_2) between (b) mantle only and combined models, (d) GPE only and combined models. The ratio gives a measure of what fraction of the total stress field is originating from the mantle sources and what part from the GPE related sources.

boundary loads. A comparison of the predicted deviatoric stresses between the combined model and the model with mantle tractions only (no GPE) (Figs 18a and b) and GPE variations only (Figs 18c and d), provides a quantitative assessment of the importance of basal tractions versus GPE variations. We compute correlation coefficients (r), given as $r = \tau \cdot \tau' / T * T'$ (Flesch *et al.* 2001; Ghosh *et al.* 2008, 2009), where τ denotes the deviatoric stress components for the combined model and τ' denotes the deviatoric stress components for the traction only or GPE only model; T, T' are the second invariants of deviatoric stresses for the combined model and

mantle traction/GPE model and * indicates simple multiplication. $\tau \cdot \tau'$ is given as

$$\tau \cdot \tau' = \tau_{\phi\phi}\tau'_{\phi\phi} + 2\tau_{\phi\theta}\tau'_{\phi\theta} + \tau_{\theta\theta}\tau'_{\theta\theta} + 2\tau_{r\phi}\tau'_{r\phi} + 2\tau_{r\theta}\tau'_{r\theta} + \tau_{rr}\tau'_{rr}. \quad (1)$$

$$T = \sqrt{T_{\phi\phi}^2 + T_{\theta\theta}^2 + T_{rr}^2 + 2(T_{\phi\theta}^2 + T_{r\phi}^2 + T_{r\theta}^2)} \quad (2)$$

The correlation coefficient measures how similar the two stress fields are in terms of style and orientation. The correlation between the stresses from mantle tractions only and the combined model is generally higher than those between GPE only and the combined models (Figs 18a and c). A ratio of the second invariant of the deviatoric stresses (T/T') between the combined model and mantle tractions only/GPE only model (Figs 18b and d) indicates the fraction of the total stress magnitudes that the two components individually constitute. For example, in Colorado Plateau, Basin and Range, Snake River Plain, the mantle traction related stresses constitute between 40–60 per cent of the total stress field, whereas GPE related stresses slightly dominate in those areas (40–80 per cent). Our results support one of the conclusions of Jones *et al.* (1996) and Humphreys & Coblentz (2007) that the tensional nature of the stresses in western United States is largely due to GPE variations.

Our current modelling attempt was to resolve the relative importance of the sources of deformation for western United States. Our methodology is novel in the sense that we incorporate lithospheric gravitational response (GPE variations) in 3-D, global self-consistent mantle convection models, in addition to including effects such as anisotropic viscosity. We include LVVs in our models, which had been deemed as potentially important in earlier studies, and also isolate the effects that these individual sources of LVVs have on the dynamics of the region. We use all the four observational constraints of geoid, dynamic topography, plate motions and deviatoric stress field and compare them quantitatively with our model predictions. We have also used the latest high-resolution tomography models available for that region. Western North America is a complex region where the sources of deformation have been debated for decades. Our models, although do not put an end to that controversy, are well equipped to address the various problems associated with this complicated region.

ACKNOWLEDGEMENTS

This work was supported by NSF grants EAR 0106892 and EAR 0910985. Software package CitcomS is maintained at CIG. Computations were done on HPC at USC. This paper benefited from comments by the associate editor and by an anonymous reviewer. We also thank B. Steinberger for helpful discussions in the initial stages of preparing the manuscript.

REFERENCES

Bai, W., Vigny, C., Ricard, Y. & Froidevaux, C., 1992. On the origin of deviatoric stresses in the lithosphere, *J. geophys. Res.,* **97,** 11 729–11 737.

Becker, T.W., 2006. On the effect of temperature and strain-rate viscosity on global mantle flow, net rotation, and driving forces, *Geophys. J. Int.,* **167,** 943–957.

Becker, T.W., 2012. On recent seismic tomography for the western United States, *Geochem. Geophys. Geosyst.,* **13,** Q01W10, doi:10.1029/2011GC003977.

Becker, T.W. & Boschi, L., 2002. A comparison of tomographic and geodynamic mantle models, *Geochem. Geophys. Geosyst.,* **3,** doi:2001GC000168.

Becker, T.W. & Faccenna, C., 2011. Mantle conveyor beneath the Tethyan collisional belt, *Earth planet. Sci. Lett.,* **310,** 453–461.

Becker, T.W. & Kawakatsu, H., 2011. On the role of anisotropic viscosity for plate-scale flow, *Geophys. Res. Lett.,* **38,** doi:10.1029/2011GL048584.

Becker, T.W. & O'Connell, R.J., 2001. Predicting plate velocities with mantle circulation models, *Geochem. Geophys. Geosyst.,* **2**(12), doi:10.1029/2001GC000171.

Becker, T.W., Schulte-Pelkum, V., Blackman, D.K., Kellogg, J.B. & O'Connell, R.J., 2006. Mantle flow under western United States from shear wave splitting, *Earth planet. Sci. Lett.,* **247,** 235–251.

Bird, P., 1998. Testing hypotheses on plate-driving mechanisms with global lithosphere models including topography, thermal structure and faults, *J. geophys. Res.,* **103,** 10 115–10 129.

Bird, P., Liu, Z. & Rucker, W.K., 2008. Stresses that drive the plates from below: definitions, computational path, model optimization, and error analysis, *J. geophys. Res.,* **113,** B11406, doi:10.1029/2007JB005460.

Bokelmann, G.H.R., 2002. Which forces drive North America?, *Geology,* **30,** 1027–1030.

Braun, J., 2010. The many surface expressions of mantle dynamics, *Nature Geoscience,* **3,** 825–833.

Chambat, F., Ricard, Y. & Valette, B., 2010. Flattening of the earth: further from hydrostaticity than previously estimated, *Geophys. J. Int.,* **183,** 727–732.

Christensen, U., 1987. Some geodynamical effects of anisotropic viscosity, *Geophys. J. R. astr. Soc.,* **91,** 711–736.

Conrad, C.P. & Lithgow-Bertelloni, C., 2002. How mantle slabs drive plate tectonics, *Science,* **298,** doi:10.1126/science.1074161.

Conrad, C.P. & Lithgow-Bertelloni, C., 2006. Influence of continental roots and asthenosphere on plate-mantle coupling, *Geophys. Res. Lett.,* **33,** L05312, doi:10.1029/2005GL025621.

DeMets, C., Gordon, R.G., Argus, D.F. & Stein, S., 1994. Effect of recent revisions to the geomagnetic reversal time scale on estimates of current plate motions, *Geophys. Res. Lett.,* **21,** 2191–2194.

English, J.M. & Johnston, S.T., 2004. The Laramide orogeny: what were the driving forces?, *Int. Geol. Rev.,* **46,** 833–838.

Fleitout, L. & Froidevoux, C., 1983. Tectonic stresses in the lithosphere, *Tectonophys.,* **2,** 315–324.

Flesch, L.M., Holt, W.E., Haines, A.J. & Shen-Tu, B., 2000. Dynamics of the Pacific-North American plate boundary in the western United States, *Science,* **287,** 834–836.

Flesch, L.M., Haines, A.J. & Holt, W.E., 2001. Dynamics of the India-Eurasia collision zone, *J. geophys. Res.,* **106,** 16 435–16 460.

Flesch, L.M., Holt, W.E., Haines, A.J., Wen, L. & Shen-tu, B., 2007. The dynamics of western North America: stress magnitudes and the relative role of gravitational potential energy, plate interaction at the boundary, and basal tractions, *Geophys. J. Int.,* **169,** 866–896.

Forte, A., Moucha, R., Simmons, N., Grand, S. & Mitrovica, J., 2010. Deep-mantle contributions to the surface dynamics of the North American continent, *Tectonophys,* **481,** 3–15.

Forte, A.M., 2007. Constraints on seismic models from other disciplines—implications for mantle dynamics and composition, in *Treatise of Geophysics,* pp. 805–858, eds Romanowicz, B. & Dziewonski, A.M., Elsevier, Amsterdam.

Forte, A.M. & Perry, H.K.C., 2000. Geodynamic evidence for a chemically depleted continental tectosphere, *Science,* **290,** 1940–1944.

Forte, A.M., Peltier, W.R., Dziewonski, A.M. & Woodward, R.L., 1993. Dynamic surface topography: a new interpretation based upon mantle flow models derived from seismic tomography, *Geophys. Res. Lett.,* **20,** 225–228.

Ghosh, A. & Holt, W.E., 2012. Plate motions and stresses from global dynamic models, *Science,* **335,** 838–843.

Ghosh, A., Holt, W.E., Wen, L., Haines, A.J. & Flesch, L.M., 2008. Joint modeling of lithosphere and mantle dynamics elucidating lithosphere-mantle coupling, *Geophys. Res. Lett.,* **35,** L16309, doi:10.1029/2008GL034365.

Ghosh, A., Holt, W.E. & Flesch, L.M., 2009. Contribution of gravitational potential energy differences to the global stress field, *Geophys. J. Int.,* **179,** 787–812.

Ghosh, A., Becker, T.W. & Zhong, S.J., 2010. Effect of lateral viscosity variations on the geoid, *Geophys. Res. Lett.,* **37,** L01301, doi:10.1029/2009GL040426.

Ghosh, A., Holt, W.E. & Wen, L., 2013. Predicting the lithospheric stress field and plate motions by joint modeling of lithosphere and mantle dynamics, *J. geophys. Res.,* **118,** 346–368.

Gilbert, L.E. & Scholz, C.H., 1994. Strain localization along the San Andreas fault: consequences for loading mechanisms, *J. geophys. Res.,* **99,** 23 975–23 984.

Gudmundsson, O. & Sambridge, M., 1998. A regionalized upper mantle (RUM) seismic model, *J. geophys. Res.,* **103,** 7121–7136.

Han, D. & Wahr, J., 1997. An analysis of anisotropic mantle viscosity, and its possible effects on postglacial rebound, *Phys. Earth planet. Inter.,* **102,** 33–50.

Heidbach, O., Tingay, M., Barth, A., Reinecker, J., Kurfeb, D. & Müller, B., 2008. The World Stress Map database release 2008, doi:10.1594/GFZ.WSM.Rel2008.

Humphreys, E. & Coblentz, D., 2007. North American dynamics and western U.S. tectonics, *Rev. Geophys.,* **45,** RG3001, doi:10.1029/2005RG000181.

Husson, L., Conrad, C.P. & Faccenna, C., 2008. Tethyan closure, Andean orogeny, and westward drift of the Pacific Basin, *Earth planet. Sci. Lett.,* **271,** 303–310.

Jackson, J., 2002. Faulting, flow, and the strength of the continental lithosphere, *Int. Geol. Rev.,* **44,** 39–61.

Jones, C.H., Unruh, J. & Sonder, L., 1996. The role of gravitational potential energy in active deformation in the southwestern United States, *Nature,* **381,** 37–41.

Jordan, T.H., 1978. Composition and development of the continental tectosphere, *Nature,* **274,** 544–548.

King, S.D. & Hager, B.H., 1990. The relationship between plate velocity and trench viscosity in newtonian and power-law subduction calculations, *Geophys. Res. Lett.,* **12,** 2409–2412.

Kreemer, C., Holt, W.E. & Haines, A.J., 2003. An integrated global model of present-day plate motions and plate boundary deformation, *Geophys. J. Int.,* **154,** 8–34.

Lebedev, S. & van der Hilst, R.D., 2008. Global upper-mantle tomogarphy with the automated multimode inversion of surface and s-wave forms, *Geophys. J. Int.,* **173,** 505–518.

Lev, E. & Hager, B.H., 2008. Rayleigh–Taylor instabilities with anisotropic lithospheric viscosity, *Geophys. J. Int.,* **173,** 806–814.

Lev, E. & Hager, B.H., 2011. Anisotropic viscosity changes subduction zone thermal structure, *Geochem. Geophys. Geosyst.,* **12**, Q04009, doi:10.1029/2010GC003382.

Lithgow-Bertelloni, C. & Guynn, J.H., 2004. Origin of the lithospheric stress field, *J. geophys. Res.,* **109,** B01408, doi:10.1029/2003JB002467.

Liu, L., Gurnis, M., Seton, M., Saleeby, J., Müller, R.D. & Jackson, J.M., 2010. The role of oceanic plateau subduction in the Laramide orogeny, *Nat. Geosci.,* **3,** 353–357.

Liu, Z. & Bird, P., 2002. North america plate is driven westward by lower mantle flow, *Geophys. Res. Lett.,* **29**(24), doi:10.1029/2002GL016002.

Livacarri, R.F., 1991. Role of crustal thickening and extensional collapse in the tectonic evolution of the sevier-laramide oro- geny, western united states, *Geology,* **19,** 1104–1107.

Mayer-Guerr, T., 2006. Gravitationsfeldbestimmung aus der analyse kurzer bahnbogen am beispiel der satellitenmissionen CHAMP und GRACE, *PhD thesis,* University of Bonn, Germany.

Nakiboglu, S.M., 1982. Hydrostatic theory of the Earth and its mechanical implications, *Phys. Earth planet. Int.,* **28,** 302–311.

Naliboff, J.B., Conrad, C.P. & Lithgow-Bertelloni, C., 2009. Modification of the lithospheric stress field by lateral variations in plate-mantle coupling, *Geophys. Res. Lett.,* **36,** L22307, doi:10.1029/2009GL040484.

Nataf, H. & Ricard, Y., 1996. 3smac: an a priori tomographic model of the upper mantle based on geophysical modeling, *Phys. Earth planet. Inter.,* **95,** 101–122.

Panasyuk, S.V. & Hager, B.H., 2000. Models of isostatic and dynamic topography, geoid anomalies, and their uncertainties, *J. geophys. Res.,* **105,** 28 199–28 209.

Platt, J.P., Kaus, B. & Becker, T.W., 2008. The mechanics of continental transforms: an alternative approach with applications to the San Andreas system and the tectonics of California, *Earth planet. Sci. Lett.,* **274,** 380–391.

Pouilloux, L., Kaminski, E. & Labrosse, S., 2007. Anisotropic rheology of a cubic medium and implications for geological materials, *Geophys. J. Int.,* **170,** 876–885.

Ricard, Y. & Vigny, C., 1989. Mantle dynamics with induced plate tectonics, *J. geophys. Res.,* **94,** 5987–6002.

Schmandt, B. & Humphreys, E., 2010. Complex subduction and small-scale convection revealed by body wave tomography of the western u.s. upper mantle, *Geochem. Geophys. Geosyst.,* **11,** Q05004, doi:10.1029/2010GC003042.

Silver, P. & Holt, W.E., 2002. The mantle flow field beneath western North America, *Science,* **295,** 1054–1057.

Simmons, N.A., Forte, A.M. & Grand, S.P., 2007. Thermochemical structure and dynamics of the african superplume, *Geophys. Res. Lett.,* **34,** doi:10.1029/2006GL028009.

Sonder, L.J. & Jones, C.H., 1999. Western united states extension: how the west was widened, *Annu. Rev. Earth planet. Sci.,* **27,** 417–462.

Spencer, J.E., 1996. Uplift of the Colorado Plateau due to lithospheric attenuation during Laramide low-angle subduction, *J. geophys. Res.,* **101,** 13 595–13 609.

Stadler, G., Gurnis, M., Burstedde, C., Wilcox, L.C., Alisic, L. & Ghattas, O., 2010. The dynamics of plate tectonics and mantle flow: from local to global scales, *Science,* **329,** 1033–1038.

Steinberger, B., Schmeling, H. & Marquart, G., 2001. Large-scale lithospheric stress field and topography induced by global mantle circulation, *Earth planet. Sci. Lett.,* **186,** 75–91.

van Summeren, J., Conrad, C.P. & Lithgow-Bertelloni, C., 2012. The importance of slab pull and a global asthenosphere to plate motions, *Geochem. Geophys. Geosyst.,* **13**(1), Q0AK03, doi:10.1029/2011GC003873.

Wesnousky, S.G. & Scholz, C.H., 1980. The craton: its effect on the distribution of seismicity and stress in north america, *Earth planet. Sci. Lett.,* **48,** 348–355.

Zhong, S., Zuber, M.T., Moresi, L.N. & Gurnis, M., 2000. The role of temperature-dependent viscosity and surface plates in spherical shell models of mantle convection, *J. geophys. Res.,* **105,** 11 063–11 082.

Zhong, S.J. & Gurnis, M., 1995a. Mantle convection with plates and mobile, faulted plate margins, *Science,* **267,** 838–843.

Zhong, S.J. & Gurnis, M., 1995b. Towards a realistic simulation of plate margins in mantle convection, *Geophys. Res. Lett.,* **22,** 981–984.

Zoback, M.D., 2000. Strength of the San Andreas, *Nature,* **405,** 31–32.

Zoback, M.D. & Zoback, M.L., 1981. State of stress and intraplate earthquakesin the united states, *Science,* **213,** 96–104.

Zoback, M.L. & Zoback, M.D., 1980. State of stressin the conterminous united states, *J. geophys. Res.,* **85,** 6113–6156.

APPENDIX A: BENCHMARKING OF GPE RELATED STRESSES

We carry out two separate benchmarking tests. In the first one, we apply shear tractions that are derived from GPE gradients (see Section 3), as surface boundary condition halfway through the lithosphere, that is up to a depth of 50 km, in a circulation model in CitcomS with a simple radial viscosity distribution. No density anomalies are included within the mantle, that is, the flow in the mantle is driven solely by these surface shear tractions. The deviatoric stresses predicted by such a model within the lithosphere are compared to the vertically integrated deviatoric stresses obtained from GPE variations in a thin sheet lithosphere model, calculated by solving a system of force balance equations as in Ghosh *et al.* (2009). The deviatoric stresses from the lithosphere model

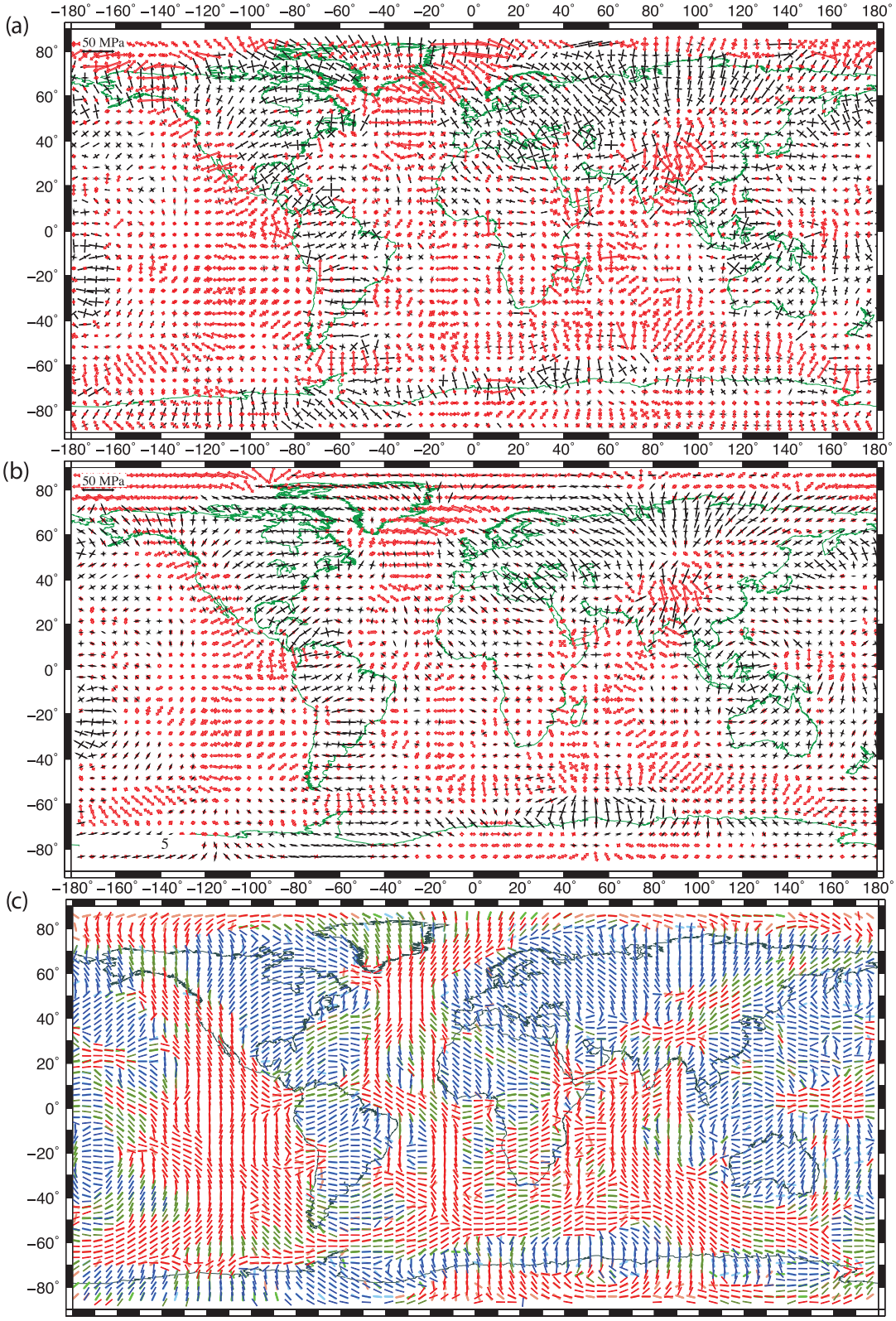

Figure A1. (a) Deviatoric stresses predicted from GPE differences via a thin sheet computation plotted every 5°. Red denotes deviatoric tension, black denotes deviatoric compression. (b) Deviatoric stresses predicted at 72 km depth via a CitcomS model where flow is set up by shear tractions, which are negative of GPE gradients at the surface. (c) Most compressive principal axes of deviatoric stress tensors from Fig. A1(a) plotted on top of the most compressive principal axes from Fig. A1(b). The different colours indicate the strain environment predicted by the deviatoric stresses. Red indicates maximum horizontal extension in a normal fault regime, blue indicates maximum horizontal compression in a thrust fault regime and green denotes maximum horizontal compressive stress direction in a strike-slip regime.

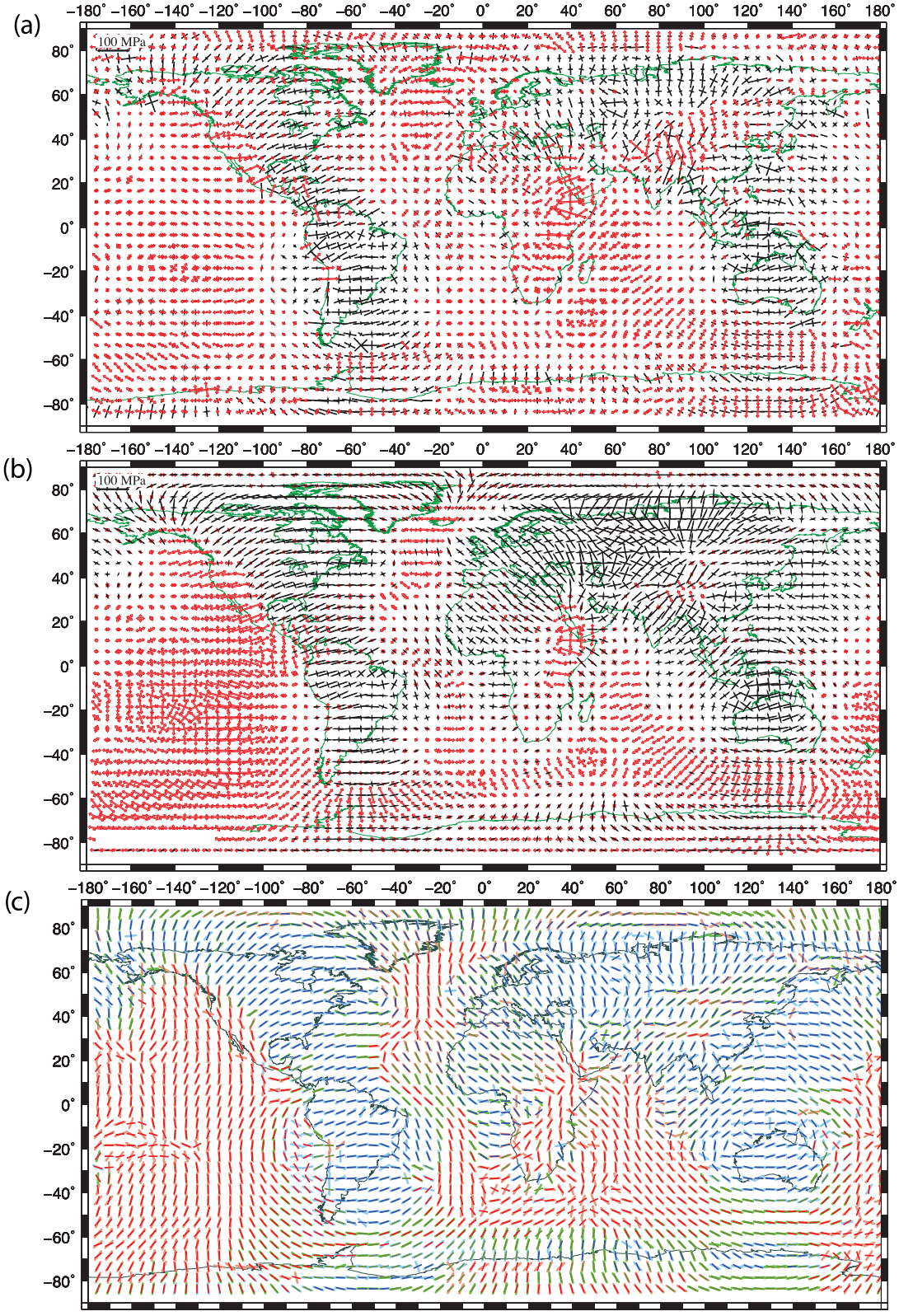

Figure A2. Same as Fig. A1, only the deviatoric stresses are from combined GPE and mantle flow.

calculations (Fig. A1a) and CitcomS calculations (Fig. A1b) are almost identical. We also show the most compressive principal stress axes from the two separate calculations (Fig. A1c) and they display a remarkable similarity both in terms of stress orientation and style. It should be noted that the deviatoric stresses predicted from the convection model are full 3-D stresses, whereas the stresses from the thin sheet lithosphere model are not. Moreover, the stresses from the lithosphere model are vertically integrated over the entire lithosphere in contrast to the stresses from flow model that are predicted at particular depths. Since the CitcomS stress predictions are 3-D,

they have three principal stress axes. Of those three axes we are plotting, the two axes that are most parallel to the horizontal.

While the above test dealt with testing the stresses from surface boundary condition alone, in the other test we benchmark the combined stresses from surface shear tractions and internal density anomalies within the mantle. This is a four-step process. In the first step, we compute shear tractions acting at the base of the lithosphere (∼100 km depth) from a mantle circulation model in CitcomS driven by SMEAN tomography with only radial viscosity variations and free slip boundary condition. In the next step, these tractions are applied at the base of the lithosphere in the thin sheet model as boundary condition (Ghosh *et al.* 2008, 2013). The resultant deviatoric stresses are the effect of density driven mantle flow only. Thirdly, these stresses are then added to the deviatoric stresses calculated from GPE variations acting on the same thin sheet lithosphere model. The linearity of the force balance equations enables us to simply add these two components in order to obtain a total stress tensor field for the entire lithosphere that is a result of both topography and shallow lithosphere density variations (GPE differences) and deeper mantle flow. In the fourth and final step, we use the same CitcomS model, from which the basal tractions were generated (that is with the same density and viscosity structure in step 1) and instead replace the free slip boundary condition at the surface with stress boundary condition. The stress boundary condition is set up as before by shear tractions, which are the negative of GPE gradients. Hence, this time the flow in the CitcomS model is driven by both mantle density anomalies and GPE variations (as in Section 4.2). The resultant deviatoric stress field is compared to the total deviatoric stress field from the lithosphere model obtained in step 3. The resultant stresses are very similar in orientation and style (Fig. A2c), although in some areas there exist differences in stress magnitudes (Figs A2a,b), which could potentially be attributed to the fact that we are comparing vertically integrated stresses with those at a particular depth.

The above benchmarking tests show that we can recover the same stress tensors if we apply them as stress boundary condition as opposed to treating the GPE related stresses in a separate model. A big advantage of this approach is that we can avoid using a separate lithosphere model and can integrate the topography and shallow lithosphere response directly in the convection model. This is especially important for very high resolution studies, particularly in subduction zones, where the thin sheet assumption may no longer hold.